Article

Cell Reports

Connectomic analysis of thalamus-driven disinhibition in cortical layer 4

Graphical abstract

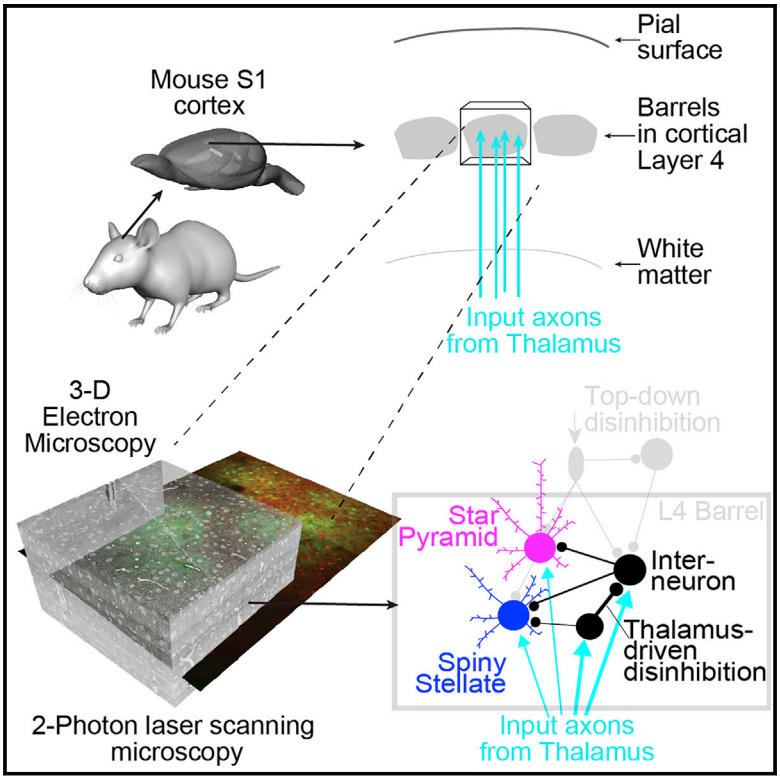

Highlights

- Thalamus directly drives a disinhibitory circuit in cortical layer 4
- Distinct interneuron input to excitatory neuron subtypes in layer 4
- Temporally precise windows of activation within layer 4 predicted from connectome
- Functional recordings support such differential activation windows within layer 4

Authors

Yunfeng Hua, Sahil Loomba, Verena Pawlak, ..., Damian J. Wallace, Jason N.D. Kerr, Moritz Helmstaedter

Correspondence

yunfeng.hua@shsmu.edu.cn (Y.H.), jason.kerr@mpinb.mpg.de (J.N.D.K.), mh@brain.mpg.de (M.H.)

In brief

Hua et al. used three-dimensional electron microscopy to determine the inhibitory interneuron connectome within layer 4 of mouse primary somatosensory cortex, discovering a directly thalamus-driven disinhibitory circuitry with target specificity for the excitatory neuronal subtypes. Functional recordings confirm the differential temporal activation windows created by this circuit.

Hua et al., 2022, Cell Reports *41*, 111476
October 11, 2022
https://doi.org/10.1016/j.celrep.2022.111476

CellPress

Cell Reports

CellPress
OPEN ACCESS

Article

Connectomic analysis of thalamus-driven disinhibition in cortical layer 4

Yunfeng Hua,[1,2,5,*] Sahil Loomba,[2,4,5] Verena Pawlak,[3] Kay-Michael Voit,[3] Philip Laserstein,[2] Kevin M. Boergens,[2] Damian J. Wallace,[3] Jason N.D. Kerr,[3,*] and Moritz Helmstaedter[2,4,6,*]

[1]Shanghai Institute of Precision Medicine, Ninth People's Hospital, Shanghai Jiao Tong University School of Medicine, Shanghai 200125, China

[2]Department of Connectomics, Max Planck Institute for Brain Research, 60438 Frankfurt, Germany

[3]Department of Behavior and Brain Organization, Max Planck Institute for Neurobiology of Behavior – Caesar, 53175 Bonn, Germany

[4]Donders Institute, Faculty of Sciences, Radboud University, Nijmegen, XZ 6525, the Netherlands

[5]These authors contributed equally

[6]Lead contact

*Correspondence: yunfeng.hua@shsmu.edu.cn (Y.H.), jason.kerr@mpinb.mpg.de (J.N.D.K.), mh@brain.mpg.de (M.H.)

https://doi.org/10.1016/j.celrep.2022.111476

SUMMARY

Sensory signals are transmitted via the thalamus primarily to layer 4 (L4) of the primary sensory cortices. While information about average neuronal connectivity in L4 is available, its detailed higher-order circuit structure is not known. Here, we used three-dimensional electron microscopy for a connectomic analysis of the thalamus-driven inhibitory network in L4. We find that thalamic input drives a subset of interneurons with high specificity, which in turn target excitatory neurons with subtype specificity. These interneurons create a directed disinhibitory network directly driven by the thalamic input. Neuronal activity recordings show that strong synchronous sensory activation yields about 1.5-fold stronger activation of star pyramidal cells than spiny stellates, in line with differential windows of opportunity for activation of excitatory neurons in the thalamus-driven disinhibitory circuit model. With this, we have identified a high degree of specialization of the microcircuitry in L4 of the primary sensory cortex.

INTRODUCTION

The logic of signal transformation in the main thalamocortical recipient layer of the mammalian brain, layer 4 (L4) of the sensory cortices, has been a major focus of functional (Brecht and Sakmann, 2002; de Kock et al., 2007; Gutnisky et al., 2017; Hubel and Wiesel, 1962; Kanold et al., 2003; Kara et al., 2002; Martinez et al., 2005; Stratford et al., 1996; Yu et al., 2016, 2019) and structural (Ahmed et al., 1994; Ahmed et al., 1997; Egger et al., 2008; Elston et al., 1997; Lübke et al., 2000; Lübke et al., 2003; Motta et al., 2019; Schubert et al., 2003; Staiger et al., 2004; Woolsey and Van der Loos, 1970) investigations. While functional studies have shown the relevance of feedforward inhibition (Bereshpolova et al., 2020; Bruno and Simons, 2002; Cruikshank et al., 2007; Gabernet et al., 2005; House et al., 2011; Pouille and Scanziani, 2001; Staiger et al., 2009), and recent recordings have demonstrated differential activation of subtypes of interneurons (Yu et al., 2016, 2019), a detailed circuit-level picture of the transformation of the thalamocortical (TC) signal onto excitatory neurons in the cortex is still lacking.

Here, we undertook a connectomic reconstruction of about 1/4th of the C2 barrel across all of L4 and parts of L3 and L5A in mouse primary somatosensory (S1) cortex using serial block-face electron microscopy (SBEM; Denk and Horstmann, 2004). The tissue had also been imaged using *in vivo* two-photon laser-scanning microscopy (Denk et al., 1990) prior to the structural experiment. We report findings about the inhibitory synaptic circuitry in L4 that is directly driven by thalamic input, unveiling a high-precision disinhibitory circuitry and a circuit-level distinction between the excitatory neuronal subtypes within L4.

RESULTS

We used SBEM (Denk and Horstmann, 2004) in continuous imaging mode (Schmidt et al., 2017) to acquire a 3D EM dataset of size 453.2 × 430.4 × 360 μm^3 at a voxel size of 11.24 × 11.24 × 30 nm^3, aligned to the C2 barrel (identified by functional two-photon imaging *in vivo*) in an 80-day old mouse (Figure 1A; tissue staining using Hua et al., 2015). The dataset extended from the lower part of L3 to the upper part of L5A (Figure 1D), containing a total of about 7,600 neuronal cell bodies. We then used our online annotation tool webKnossos (Boergens et al., 2017) to reconstruct the upward pointing (apical) dendrites of n = 1,976 neurons in a fraction of the dataset with optimal staining and image alignment (corresponding to about 1/4th of a barrel). The two primary excitatory neuron (ExN) cell types within L4, spiny stellates (SpS) and star pyramidals (StP) (Feldmeyer et al., 1999; LeVay, 1973; Lorente De No, 1938; Lübke et al., 2000; McCormick et al., 1985; Simons and Woolsey, 1984; White, 1978; Woolsey et al., 1975), were

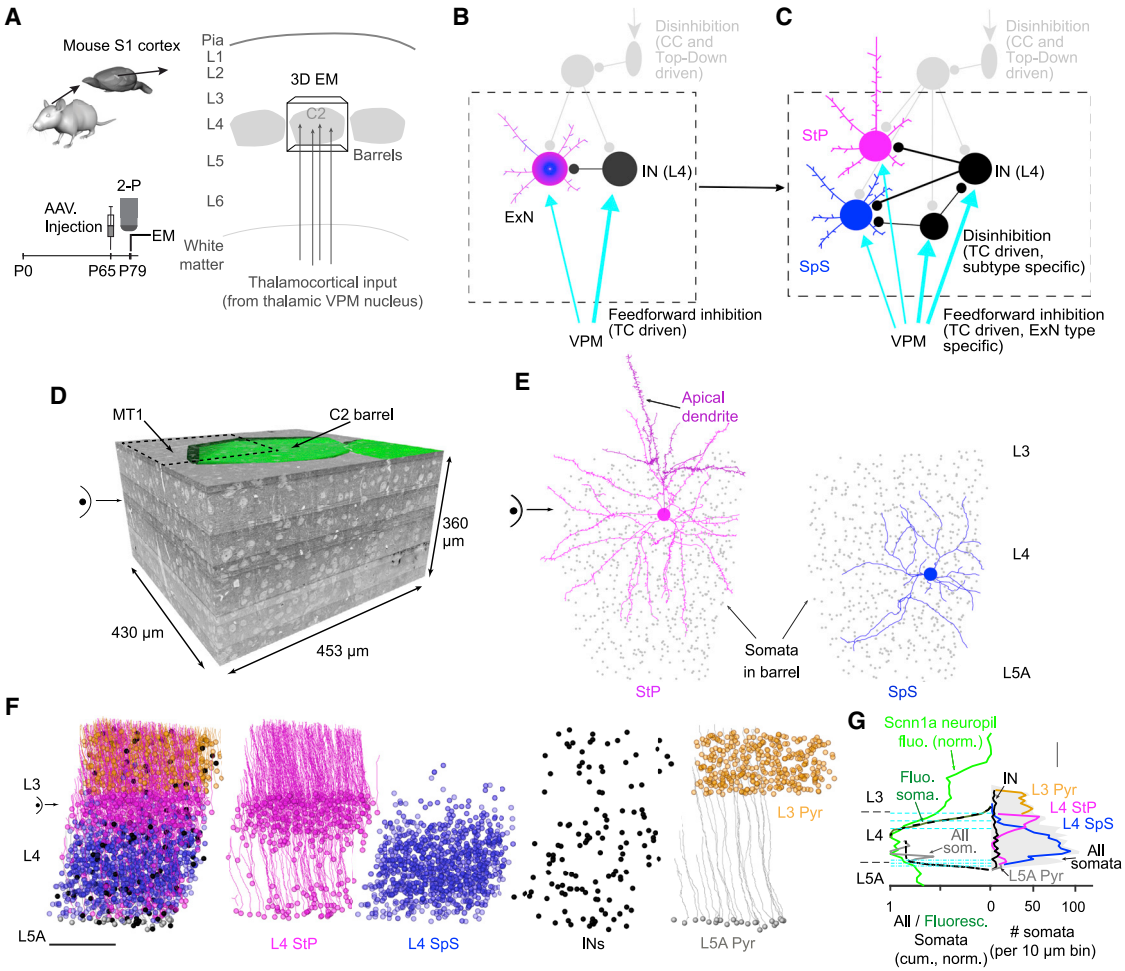

Figure 1. Connectomic analysis of neuronal circuitry in cortical layer 4 using 3D electron microscopy

(A) Experimental design: injection of L4-targeted viral construct, functional two-photon (2P) recording experiment, and 3D-EM experiment targeted to the C2 barrel in mouse S1 cortex.

(B) Current model of thalamocortical and intracortical circuitry in which thalamic afferents drive intracortical feedforward inhibition, while intracortical disinhibitory circuits are triggered from top-down and/or intracortical sources.

(C) Circuit found in this study with thalamus-driven disinhibition on top of subtype-specific feedforward inhibition yielding a high-precision circuitry already within L4.

(D) 3D-EM dataset spanning lower L3, L4, and upper L5A. Location of C2 barrel obtained from functional recordings superimposed (green). Note that circuit analysis was performed in a volume sized 229 × 217 × 300 µm (motor tile [MT] 4) corresponding to about 1/4th of the C2 barrel in the tangential plane but spanning all of L4 (dashed region).

(E) Main excitatory cell types in L4: star pyramidal (StP) and spiny stellate (SpS) neurons. Note lack of apical dendrite for SpS cells (right).

(F) Distribution of L4 StP neurons, SpS neurons, INs, and L3 and L5A pyramidal neurons (L3 Pyr, L5A Pyr), respectively. Note slight tilt of cortical axis evident from direction of apical dendrites; data in (G) were projected onto this axis.

(G) Distribution of cell types along cortical axis shows layering within L4 with bottom two-thirds dominated by SpS cells and top third by StP cells. Note homogeneous overall distribution of INs. Definition of layer borders (dashed lines) via increase of fluorescent somata (L3 → L4, green, 10th percentile of sigmoid fit) and increase of soma density (L5A → L4, gray, 50th percentile). Soma densities (right) shown per 10 µm along cortical axis, normalized to total number of somata. Scale bars (F and G) 100 µm.

distinguishable based on the existence or lack of an apical dendrite (Figure 1E). The two ExN cell types showed surprisingly clear depth separation within L4: SpS occupied the lower two-thirds of L4 (lower ~124 µm), while StP were found primarily in the upper third of L4 (upper ~52 µm; Figures 1F and 1G; fraction of ExN types in L4: 71% SpS, 29% StP). The distribution of interneurons (INs, Figure 1G) was rather homogeneous over the depth of L4. At the bottom of L4, we used the steep drop of cell density from L4 to L5A as definition of the layer border (Figures 1F and 1G). This included a set of apical dendrite-bearing neurons at the bottom of the thus-defined L4, which we labeled as StP, but which could also be L5A pyramidal neurons. We also found evidence that StP neurons had a higher number of somatic input synapses than SpS, yielding a slightly higher fraction of inhibitory synaptic inputs (Figure S3).

Thalamus-driven interneurons in L4

We next aimed to identify the thalamus-driven INs in L4 (Bagnall et al., 2011; Cruikshank et al., 2007; Porter et al., 2001; Swadlow, 2003; Yu et al., 2016, 2019). For this, we first identified all INs (Figure 2A; n = 58, of these n = 52 in C2 barrel), reconstructed their dendrites (Figure 2B; only C2 INs), and identified all input synapses made onto all their dendrites (total n = 147,619 synapses onto n = 52 INs, Figure S1; n = 2,839 ± 1,555 input synapses per IN, range 1,113–6,904 for INs with sufficiently complete dendrite, Figures 2B–2D and S1B). We then determined for each synapse whether it was a thalamocortical (TC) synapse originating from a thalamic neuron in the ventral posteromedial nucleus (VPM) or not (Figure 2C, total of n = 2,453 TC synapses [average of 1.6%]; criteria were size and synapse number of presynaptic boutons along the putative TC axon according to Bopp et al., 2017; Motta et al., 2019). This allowed a clear distinction of INs with substantially higher TC input (n = 8 of 53 INs with more than 5% TC input synapses corresponding to at least n = 98 TC input synapses per IN, more than 3-fold the average TC input) from all other INs that received less than 3% TC input (Figures 2D and 2E). For the remainder of the manuscript, we denote this type of IN with distinctively high TC input as "thalamocortical interneurons" (TC-INs). Interestingly, the degree of TC input was highly distinctive also among those INs that extended a large fraction of their dendrites within the barrel (Figures 2F and 2G): while all TC-INs had at least 70% of their dendrites in the barrel (and received 6% ± 1% TC input, n = 8), a second group of INs with more than 70% of their dendrites in the barrel received 10-fold less TC input (0.6% ± 0.5%, n = 14; Figure 2F).

We then reconstructed axons of all INs (Figures 2G–2I and S2) and found that the TC-INs all have axons that were largely restricted to the home barrel, unlike all other INs (with the exception of neurogliaform INs that had very local and barrel-related axon but received no TC input) (Figures 2H and 2I). We can thus conclude that strong TC synaptic drive converges exclusively onto barrel-related INs (Koelbl et al., 2015) whose dendrites and axons are largely restricted to the home barrel (Figure 2I) and which constitute about 15% of all INs in L4.

Excitatory targets of TC interneurons

Then, we analyzed the excitatory targets of the TC-INs (Figure 3). TC-INs targeted somata with 23% ± 8% of their output synapses (range 14%–42%, n = 8; Figure 3A). When we identified all the ExNs innervated at their somata by TC-INs (Figure 3B), we found that some TC-INs predominantly innervated SpS, while other TC-INs innervated both SpS and StP, roughly according to the prevalence of these ExN subtypes in the barrel (Figure 3C). Using this criterion, we separated the TC-INs into two subtypes depending on their preference to innervate the ExN subtypes in L4. The axonal projections of these TC-IN subtypes seemed to correspond to the layered arrangement of ExNs in L4: one TC-IN subtype extended their axons in the lower 2/3 of the barrel, in which predominantly SpS reside (Figure 3C, compare to Figure 1F), while the other TC-IN subtype extended their axons across the entire height of the barrel, innervating both SpS and StP. We therefore call the one subtype of TC-INs lower-barrel INs (L-BINs) and the other whole-barrel INs (W-BINs).

Thalamic input to TC interneurons

When quantifying the TC input onto W-BINs and L-BINs, we found that W-BINs received 2.3 ± 1.8 TC synapses per TC axon to IN pair (evaluated using 20 fully reconstructed TC axons), while L-BINs received 1.4 ± 0.7 TC synapses per axon per cell (n = 31 and n = 33 connections, respectively, $p < 0.02$, Wilcoxon rank-sum test; Figure 3D). While mapping these TC synapses to the L-BINs and W-BINs, we had further noticed that in some cases, TC axons made several synapses onto the same IN dendrite in close proximity (Figure 3E; see Bagnall et al., 2011; Cruikshank et al., 2007; Porter et al., 2001; Sun et al., 2006; Yu et al., 2016). When quantifying the fraction of TC synapses made in such a clustered configuration, we found a clear difference between the W-BINs (with 28% ± 5% clustered TC synapses) and L-BINs with 2-fold less clustering (13% ± 1%, p = 0.029, Wilcoxon rank-sum test; Figure 3F). Since this difference in strength and clustering of TC synaptic innervation had not been used for defining the subtypes of W-BINs vs. L-BINs, it already served as a first indication of systematic connectomic difference of these IN subtypes.

Interneuron-to-interneuron connectivity

We then wanted to understand the connectivity between INs within the barrel. For this, we identified all contacts between all IN axons (n = 30 INs with at least 1.5 mm axonal path length reconstructed; Figure S2) and all IN somata and dendrites and determined whether there was a chemical synapse between them (Figures 4A and 4B). The resulting 30 × 43 IN-to-IN connectome (Figure 4B) showed that (1) already among the TC-INs, substantial disinhibitory circuitry exists (Figure 4C); (2) the thalamus-driven disinhibitory circuit is strongly directed from L-BINs to W-BINs with 10-fold less innervation in the opposite direction (3.8 ± 4.1 synapses per connection vs. 0.38 ± 0.89 synapses per connection, n = 16, p = 0.002, Wilcoxon rank-sum test; Figures 4D and 4E); (3) L-BINs receive the least inhibition from any other of the INs (Figure 4E).

Possibility of gap junctional coupling

In addition to chemical synaptic connectivity, L4 INs were shown to exhibit electrical synaptic coupling during development (Beierlein et al., 2000, 2003; Connors, 2017; Galarreta and Hestrin, 1999; Gibson et al., 1999; Hatch et al., 2017; Hestrin and Galarreta, 2005; Pernelle et al., 2018). While the direct detection of gap junctions is not possible in EM data of the utilized resolution, a necessary condition for gap junctional coupling between neurons is that their dendrites (or somata) form direct appositions (without glia or other neurons in between; Figure 5A). We therefore analyzed the degree of direct dendro-dendritic touch between all INs as an upper bound on the number of appositions per IN pair at which gap junctions could in principle be formed (Figure 5B). While IN dendrites did form direct appositions, only 3% (n = 31 of 946) of IN pairs had more than one apposition, and 87% (n = 822 of 946) had no apposition at all, excluding gap junctional coupling in these IN pairs. When analyzing the dendro-dendritic touches for IN subtypes (Figure 5C), we found that L-BINs (n = 4/6 pairs) were the only IN types in which a majority of IN pairs within the type formed direct dendro-dendritic touches. No other IN type or combination of IN types did so

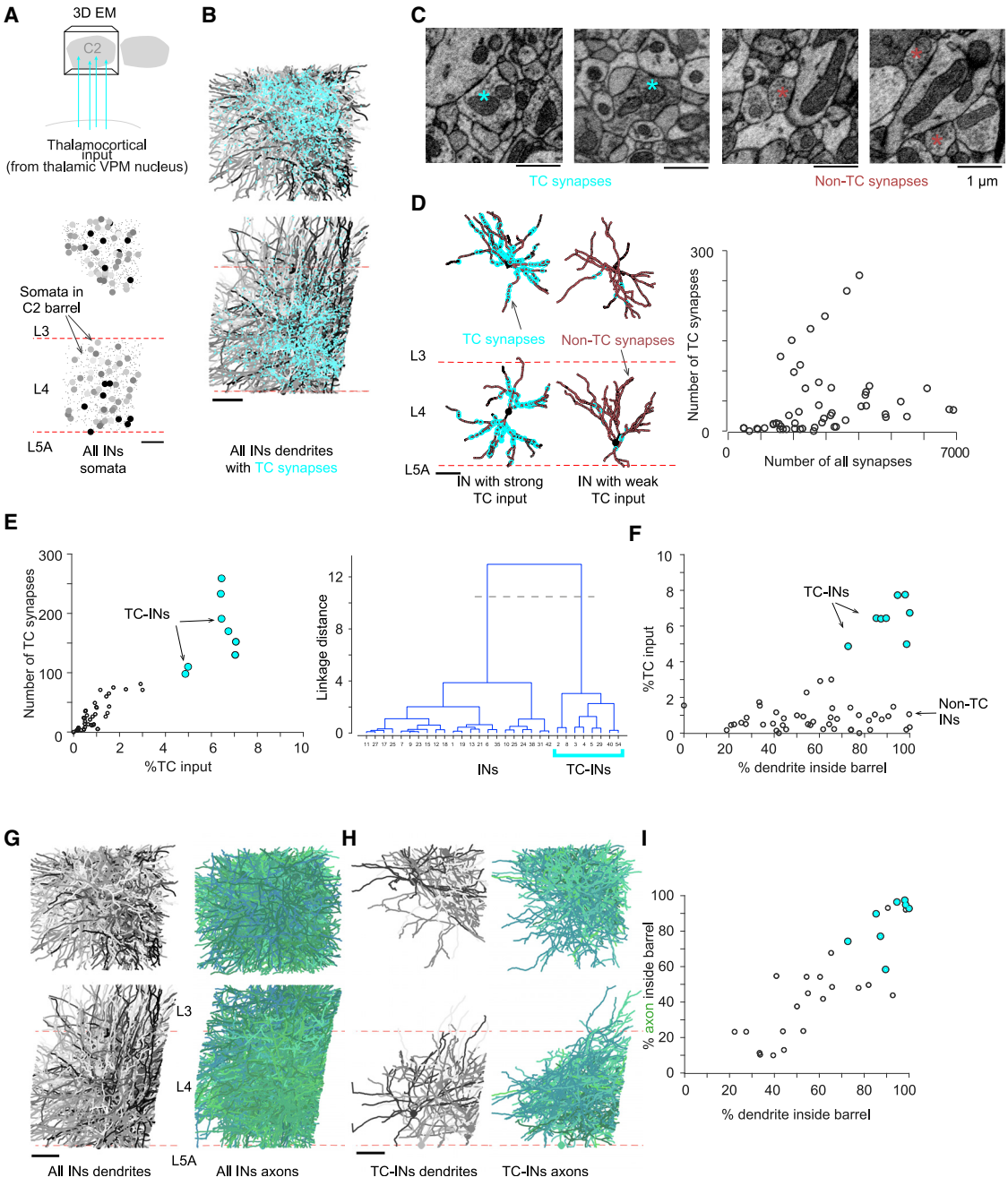

Figure 2. Thalamus-driven interneuron subtypes in L4

(A) Spatial distribution of the somata of all INs within the L4 barrel.

(B) Reconstructions of all dendrites (gray-black) of all INs; superimposed are all n = 2,453 thalamocortical (TC) synapses from the ventral posteriomedial (VPM) nucleus (cyan dots) made onto all INs.

(C) Examples of EM cross-sections showing synapses made onto IN dendrites by TC (cyan asterisk) and non-TC (brown asterisk) boutons. TC boutons are large and make multiple spine-head synapses (Bopp et al., 2017; Motta et al., 2019).

(D) Example dendrite reconstructions of IN subtypes receiving strong (left) and weak (right) TC input (TC synapses shown as cyan circles; non-TC synapses shown as brown dots). Right: distribution of all TC input synapses and all input synapses received per IN (n = 53 INs).

(E) Cluster analysis for identification of INs receiving substantial TC input ("TC-INs," shown as cyan spheres, bottom). Right: hierarchical clustering analysis to identify two groups of INs.

(F) Fraction of TC synapses received compared with extent of dendrite path length within the home barrel per IN. Note that even for INs with more than 70% of their dendrite extended in the L4 barrel, amount of TC input varies 10-fold between TC-INs (6% ± 1% TC input, n = 8) and other INs (0.6% ± 0.5% TC input, n = 14).

(G–I) Reconstructions of dendrites (gray-black) and axons (green) of all INs (G) compared with "TC-INs" (H) indicating that TC-INs also restrict their axonal output to the barrel (Koelbl et al., 2015) (I).

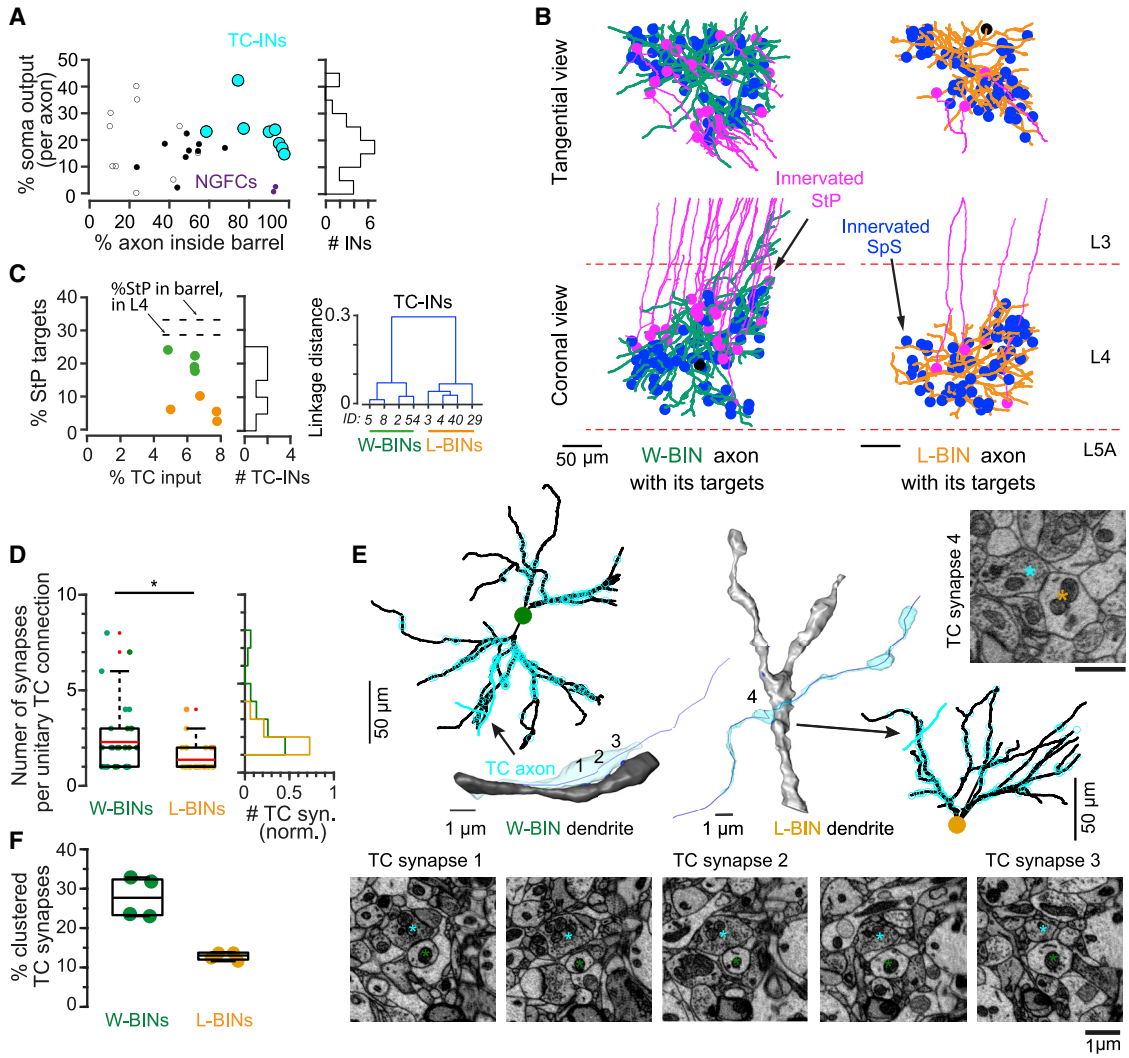

Figure 3. Connectomic subtypes of TC interneurons in L4

(A) Target preference of L4 INs to innervate somata of ExN. Note that all TC-INs make 15%–40% of their output synapses onto cell bodies (1,420 of 6,839 output synapses). Two barrel-restricted INs with no TC input and no soma targeting were identified as neurogliaform cells (NGFCs; dark purple spheres; see Figure S1). Full circles, data from fully annotated IN axons; open circles, data from randomly sampled axonal output synapses of INs.

(B) Examples of two TC-INs with all innervated postsynaptic ExN somata shown (blue: SpS somata; magenta: StP somata shown with their apical dendrite). Note innervation of both SpS and StP for TC-IN shown on the left, while strong bias for innervation of SpS for TC-IN shown on the right.

(C) Cluster analysis used to distinguish subtypes of TC-INs based on their innervation of postsynaptic ExN types: first group that innervates both StP and SpS somata ("W-BINs," green circles, top), close to a homogeneous sampling of available ExN types, and second group that suppresses StP innervation 3.5-fold (21% ± 3%, N = 4 vs. 6% ± 3%, N = 4, p = 0.03, Wilcoxon rank-sum test) and predominantly innervates SpS somata ("L-BINs," orange circles, bottom). Note this preferential innervation goes along with a height-restricted axon for L-BINs (Figure S2C).

(D–F) Analysis of TC input onto W-BINs and L-BINs shows larger number of synapses per TC axon-to-W-BIN connection (D), 2.3 ± 1.8 TC synapses per TC axon-to W-BIN pair vs. 1.4 ± 0.7 TC synapses per TC axon-to-L-BIN pair (n = 31 and n = 33 connections, respectively, $p < 0.02$, Wilcoxon rank-sum test) and (E) more synapse clustering (bottom, three consecutive synapses by same TC axon) compared with single synaptic innervations (top right). Quantification (F) shows about 2-fold difference in degree of synaptic clustering of TC input onto W-BINs vs. L-BINs (28% ± 5% of TC innervations, n = 4 vs. 13% ± 1%, n = 4, p = 0.029 Wilcoxon rank-sum test). Note that this difference in strength and clustering of TC input was not used for the definition of L-BINs vs. W-BINs in (A)–(C).

(only types with at least four INs analyzed). Since the degree of gap junctional coupling among INs in L4 had been reported to occur between about 2/3 and 3/4 of the INs (Beierlein et al., 2000, 2003; Gibson et al., 1999), L-BINs are a possible candidate for such coupling. For other IN types, 56%–100% of INs within these groups had no dendro-dendritic touch (Figure 5D), excluding the possibility that strong and prevalent electrical coupling exists among these other IN neuron populations. Notably, when analyzing all TC-INs together (combination of W-BIN and L-BIN), only a minority of IN pairs formed direct appositions (n = 13 of 28), further indicating the relevance of the differentiation between L-BINs and W-BINs.

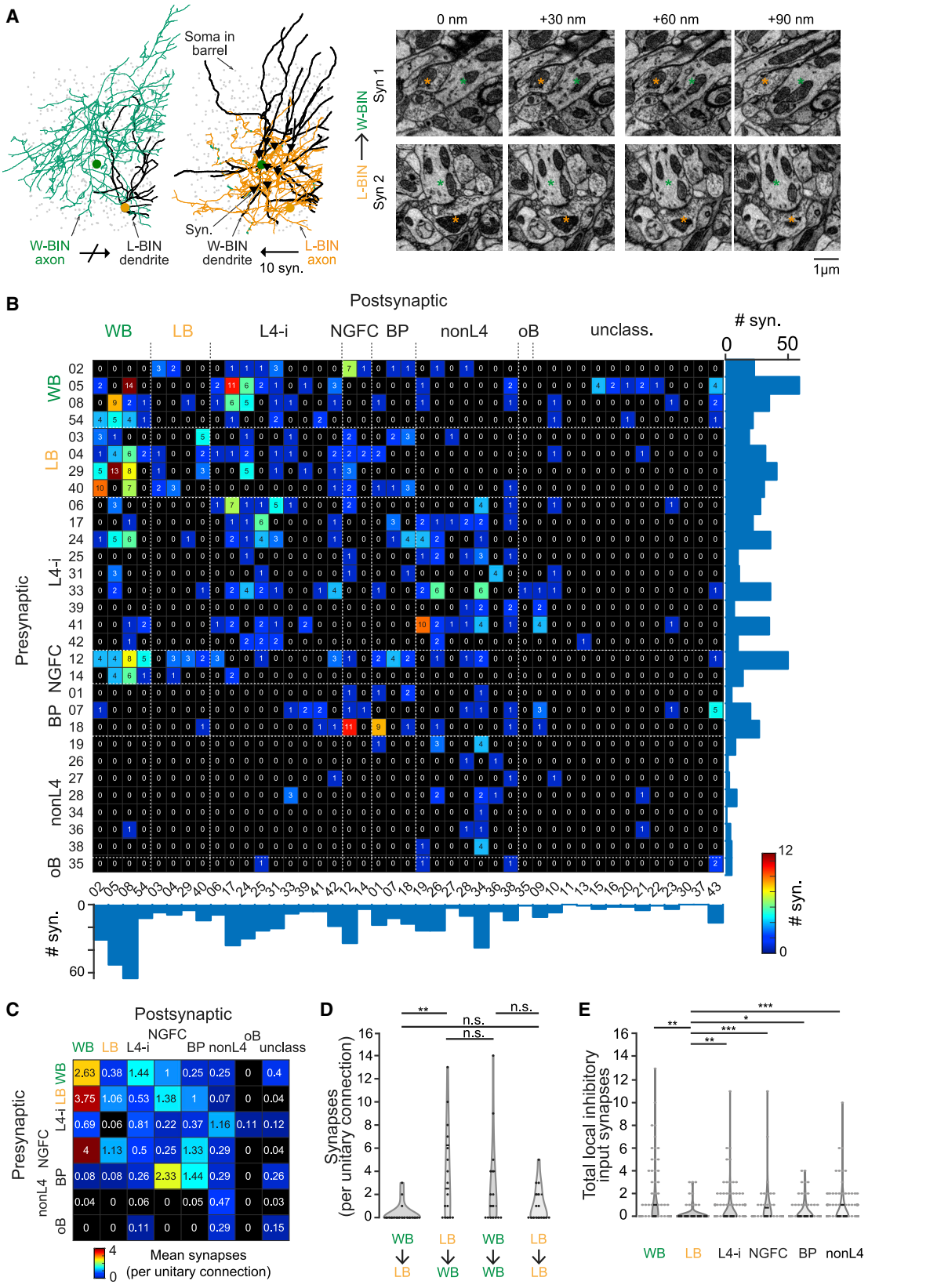

(legend on next page)

Summary of connectomic IN types

To recapitulate, the finding of a directed chemical disinhibitory circuit between L-BINs and W-BINs was surprising for two reasons: first, disinhibitory circuitry has so far been proposed to be involved in intracortical (Gainey et al., 2018; Karnani et al., 2016; Pfeffer et al., 2013; Rikhye et al., 2021; Xu et al., 2013; Yu et al., 2016, 2019) and top-down (Lee et al., 2013; Williams and Holtmaat, 2019) processing, but not for the earliest stage of cortical activation from the thalamus. Secondly, the subtype specificity of this circuitry implies a relation between the excitatory output selectivity and disinhibitory connectivity: those TC-INs that innervate all types of ExNs in the barrel (W-BINs) are unidirectionally inhibited by those TC-INs that preferentially target spiny stellates (L-BINs). Furthermore, the lack of disinhibitory input onto L-BINs but not W-BINs sets the L-BINs apart as a strong inhibitory circuit component, which itself does not receive substantial inhibition. Rather, the data on dendro-dendritic touch may indicate that L-BINs correspond to INs that were reported to be electrically coupled among each other (Beierlein et al., 2000, 2003; Gibson et al., 1999).

Sequence of thalamocortical innervation

We next investigated the TC input axons converging on the L4 circuit in more detail from the TC axon perspective (Figure 6). For this, we reconstructed 20 TC axons (identified as originating in the VPM nucleus by their trajectory from the white matter, myelination until entering L4, and features of axonal boutons; see Bopp et al., 2017 and Motta et al., 2019; Figure S4A) and identified all of their output synapses and the types of synaptic targets (Figures 6A–6C). TC axons (n = 20 axons, total length: 16.22 mm, synapse density: 0.23 ± 0.05 per μm; 3,566 output synapses total) made 4% ± 2% (n = 20) of their synapses onto the shafts of smooth dendrites; all others (96%) were onto spines of spiny dendrites. TC axons and their synapses yielded a substantial gradient of TC innervation from lower to upper L4 (Figures 6C and S4B; see Motta et al., 2019 and Oberlaender et al., 2012).

When differentiating the TC innervation of SpS and StP (Figure 6C), SpS and StP did not differ in the number of TC input synapses they received (1.18 ± 0.50 synapses [n = 22] per TC-to-StP connection versus 1.33 ± 0.83 [n = 27] per TC-to-SpS connection, Wilcoxon rank-sum test, p = 0.47; Figures 6A and 6B). Synapse size also did not differ between TC synapses onto SpS and StP ($p > 0.05$, n = 17 StP, n = 40 SpS; Figures S4C and S4D).

We found, however, that TC axons sequentially activate first SpS and then StP. The peak of these innervations is offset by at least 100 μm along the TC axon (Figure 6C; pooled innervations; for detailed analysis, see below). Notably, the TC innervation of INs aligned with the position of TC synapses onto SpS (Figure 6C; offset less than 20 μm). With this, we found that the layering of excitatory cell bodies in L4 yielded a sequential TC activation of these ExN populations, in addition to the differential innervation by subtypes of INs (Figure 2).

We then investigated how the INs innervated by TC axons projected back into the excitatory circuit in L4 (Figures 6D–6G). Feedforward inhibition (FFI) has been described as a hallmark of TC processing (Agmon and Connors, 1991; Bruno and Sakmann, 2006; Bruno and Simons, 2002; Gabernet et al., 2005; Porter et al., 2001; Temereanca and Simons, 2004; Torii and Levitt, 2005; Yu et al., 2016, 2019), but experiments were so far not able to discern whether this FFI was a population effect or whether it operated at the precision of cellular FFI (cFFI; Schmidt et al., 2017). Here, we found the cFFI configuration in at least 95% of TC-to-ExN connections were matched by at least one cFFI connection (evaluated in detail for three TC axons; Figure 6F; n = 135 TC-to-ExN synapses, n = 17 TC-to-IN synapses, n = 368 IN-to-ExN synapses with 103 of 108 excitatory targets; see STAR methods). Notably, for these cFFI configurations, the TC synapses innervating the INs were spatially aligned with the output to SpS, but 122 μm offset from the synapses onto StP, which were also innervated by cFFI (Figures 6F and 6G; Wilcoxon rank-sum test $p < 10^{-10}$ for output to INs vs. StP; $p < 10^{-18}$ for SpS vs. StP; position of output to INs and SpS was indistinguishable, Wilcoxon rank-sum test, $p > 0.9$). The previous results from cFFI in rat medial entorhinal cortex (Schmidt et al., 2017) had indicated that such a sorted axonal innervation could efficiently control postsynaptic excitatory activity if the presynaptic excitatory axon was small and had moderate action potential (AP) conduction velocity. For the TC axons, after myelination ended, we found diameters of 0.29 ± 0.10 μm (mean ± SD, n = 3) within L4 (Figures 6H and 6I). This would indicate a higher conduction velocity, so conduction-based delays may be smaller than in medial entorhinal cortex (Schmidt et al., 2017).

Circuit-based prediction of differential L4 activation

Our key circuit findings in L4, the direct TC-driven disinhibitory circuitry with selective inhibition of SpS vs. StP targets, would

Figure 4. IN-to-IN connectome in L4

(A) Example reconstructions of pair of W-BIN (i02) and L-BIN (i40) showing inhibitory synapses (black triangles): no inhibitory synapse in the W-BIN-to-L-BIN connection (left), but n = 10 synapses in the reciprocal connection (right). Bottom: examples of EM cross-sections showing synapses made by L-BIN axon (orange asterisk) onto W-BIN dendrite (green asterisk).

(B) 30 × 43 IN-to-IN connectome; numbers in connectome represent synapses per directed connection. Zeros mean no synapse found after examination of all outgoing connections. Only INs with at least 1.5 mm axon length shown as presynaptic (see IN gallery in Figure S2; row/column indices correspond to IN IDs in gallery). WB, whole-barrel IN (W-BIN); LB, lower-barrel IN (L-BIN); L4-i, L4-related IN; NGFC, neurogliaform cell; BP, bipolar IN, nonL4, non-layer-related IN; oB, neighboring barrel IN, unclass, INs with less than 1.5 mm axon (see Table S1).

(C) 7 × 8 IN-type to IN-type connectome, from aggregation of blocks in (B). Note directed L-BIN-to-W-BIN inhibition that is about 10-fold stronger than inverse direction; see (D). Numbers in connectome indicate average number of synapses per pair of pre- and postsynaptic INs.

(D) Comparison of number of synapses per L-BIN-to-W-BIN connection vs. the reverse direction (Wilcoxon rank-sum test, $p < 0.01$) and within each group (W-BIN to W-BIN vs. L-BIN to L-BIN, p = 0.32, Wilcoxon rank-sum test).

(E) Total inhibitory input synapses per INs of each subtype, aggregated over all inputs from INs of other subtypes. Inhibition onto L-BINs was significantly lower than inhibition received by other IN subtypes (W-BINs vs. L-BINs $p < 0.001$, L4-INs vs. L-BINs $p < 0.01$, NGFCs vs. L-BINs $p < 0.001$, bipolar INs vs. L-BINs $p < 0.05$, nonL4 INs vs. L-BINs $p < 0.001$, Wilcoxon rank-sum test).

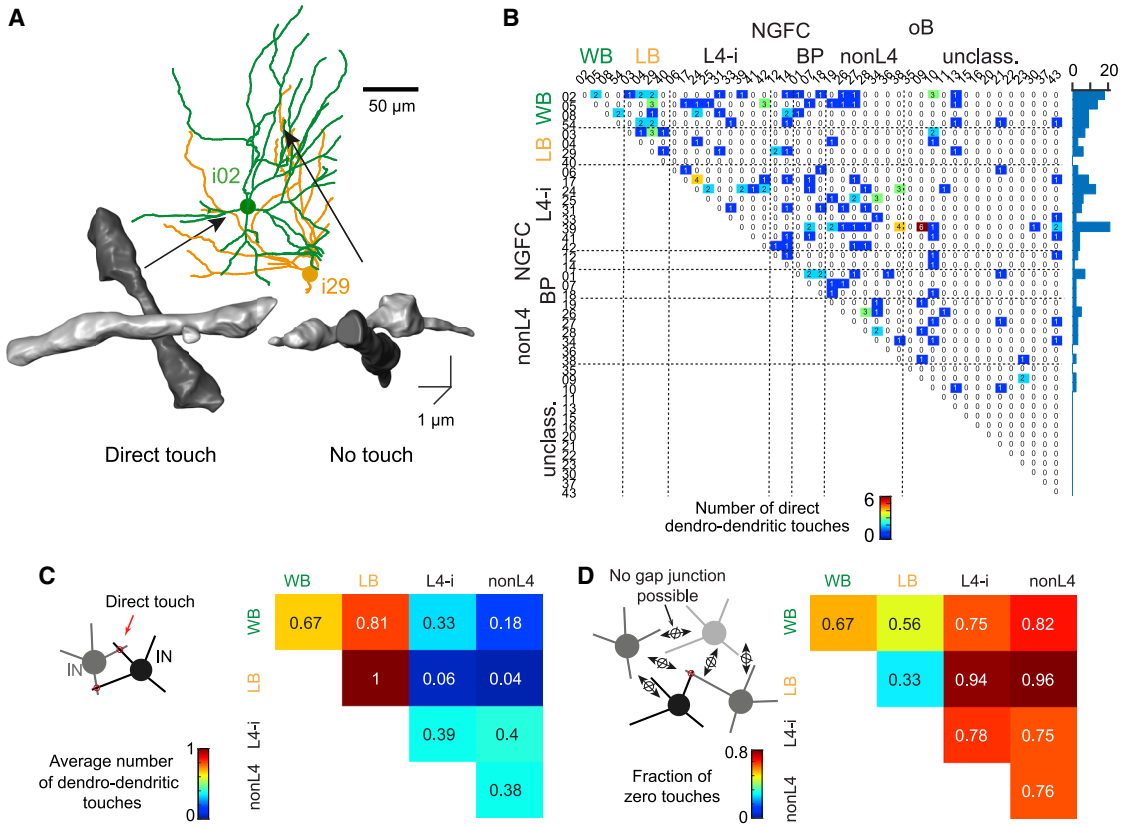

Figure 5. Dendro-dendritic touch as prerequisite of gap junctional coupling

(A) Example dendrite reconstructions of IN pair for which two apparent dendro-dendritic touches were found (dendrites closer than 1 µm).

(B) Frequency of direct dendro-dendritic touch between IN dendrites (dendrite contactome). Note dominance of zero or one-contact cell pairs (97%, n = 915 of 946).

(C) Same as (B) aggregated for IN types reporting the average number of dendro-dendritic touches per IN cell pair within and across IN types. Only IN types with at least four INs are shown.

(D) Fraction of IN pairs for which no dendro-dendritic contact was found. Note that only for L-BINs, a majority of IN pairs within each type had at least one touch. In all other IN types, gap junctional coupling cannot occur in a majority of within-type IN pairs (Beierlein et al., 2000; Gibson et al., 1999).

allow the following predictions about functional activation in L4 by sensory stimuli (Figure 7). In the case that only W-BINs but not L-BINs become activated by TC input (which could be plausible via the highly clustered TC input to W-BINs, but not L-BINs; Figure 7B), a narrow window of activity would be predicted both in SpS and StP targets, and the activity of StP could even be lower or shorter than SpS if the conduction delay effects matter in the circuit. In case of selective TC activation of L-BINs (Figure 7C), the lack of cFFI onto StP would predict a broad window of activation, potentially with very strong responses, in StP, while SpS would remain briefly activatable, only, given the selective cFFI of L-BINs onto SpS but not StP.

In case of combined activation of L-BINs and W-BINs, however (Figure 7A), the specific circuitry in L4 would predict a brief activation in SpS that is curtailed strong cFFI from both L-BINs and W-BINs. Similarly, StP would initially receive strong cFFI, potentially suppressing immediate activation. After strong activity of L-BINs has occurred, however, the targeted inhibitory circuit from L-BINs to W-BINs would predict a strong reduction in W-BIN activity. With this, the cFFI onto StP would be lifted, and StP could show strong activation by its TC input. This would yield a selective activation of L4 ExNs: SpS would only briefly activate, but StP would become strongly active after a brief delay of potentially a few milliseconds.

We next examined the functional consequences of the differential connectivity by L- and W-BINs and the feedforward inhibitory circuit described above for StP and SpS neurons. First, we identified the neurons for which we had functional data from the 2-P imaging experiment in the population of neuronal somata reconstructed from the SBEM data (Figure 7D). The functional data consisted of a total of nine fields of view, each containing an average of 5.6 ± 2.1 neurons. For each field of view, we recorded between 33 and 79 (mean ± SD, 54.2 ± 18.0) trails of whisker deflection (Figure 7E), resulting in a population of 42 neurons in total, of which 24 were StP and 18 were SpS at different cortical depth (Figure 7F). The neuronal spiking from the Ca^{2+}-traces recorded was inferred by a previously published algorithm (Greenberg et al., 2018) based on a biophysical model calibrated with cell-attached measurement under the same experimental conditions (Figure S5). Obtained AP raster plots and peri-stimulus time

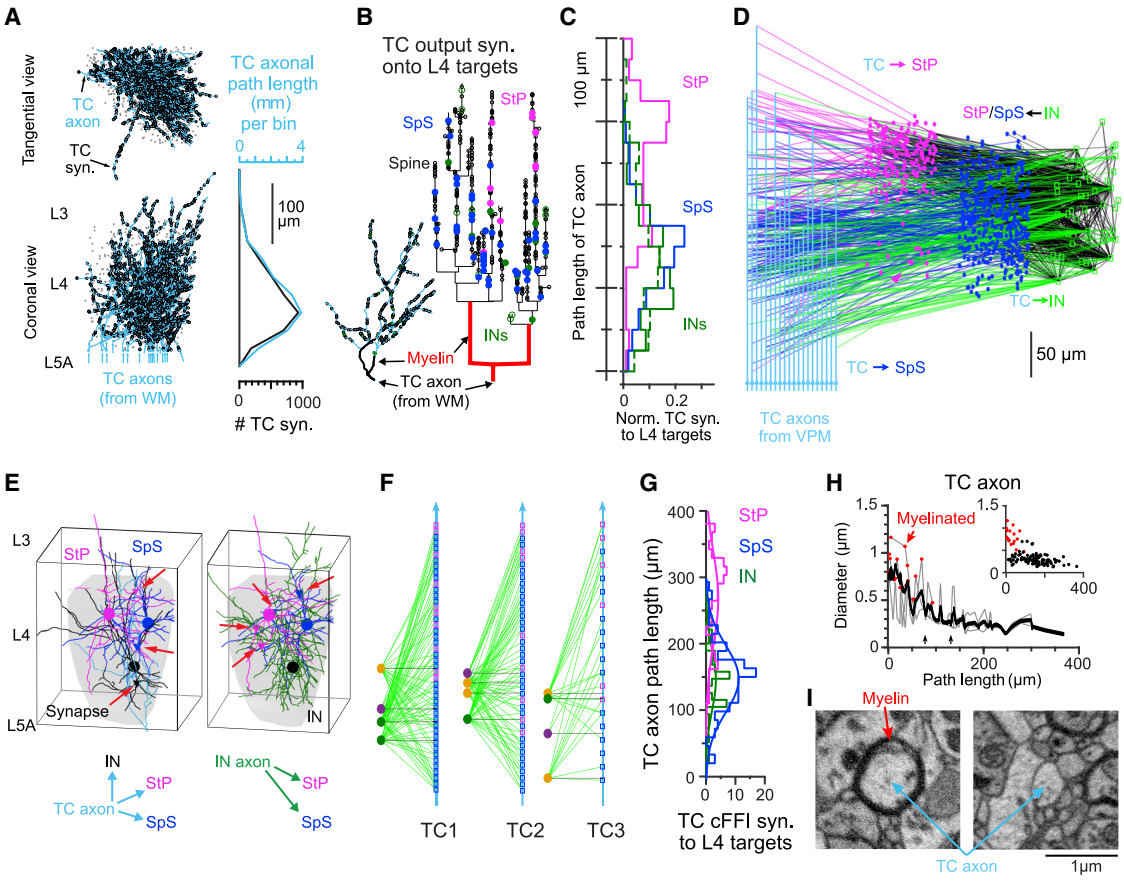

Figure 6. Thalamocortical innervation, cellular feedforward inhibition, and axonal synapse sorting

(A) Projection of 20 TC axons into the barrel and distribution of TC path length and synapses along cortical axis, yielding a substantial TC synaptic gradient in upper L4; see Motta et al. (2019) and Figure S4 for TC definition.

(B) Position of output synapses along one TC axon shown in axonogram as function of axonal path length (inset: single TC axon reconstruction). TC synapses onto INs (green; open circles, smooth dendrites; filled circles, identified INs) and ExN subtypes (StP, magenta; SpS, blue) showing synaptic sorting according to postsynaptic cell type.

(C) Ensemble distribution of output synapses from n = 20 TC axons. Note overlap of TC-to-IN with TC-to-SpS innervation, offset from TC-to-StP innervation (offset of peaks, 117 µm between IN and StP vs. 17 µm between IN and SpS). Dashed green: output to smooth (IN) dendrites without identified IN soma in barrel.

(D) Circuit diagram between 20 thalamocortical axons (cyan lines), 43 INs (green squares), 375 StP (magenta spheres), and 964 SpS targets (blue spheres) (3,089 synapses total) indicating feedforward-inhibition (FFI) circuits with differential TC synapse positions. Arrow color indicates the corresponding directed input from TC to StP (magenta), TC to SpS (blue), TC to INs (green), and INs to StP/SpS (black).

(E) Cellular-level precision of FFI-triads (red arrows indicate synapse positions) in TC-to-L4 circuits. Gray shading corresponds to barrel volume as in Figure 2.

(F) INs (circles, left) innervated by a given TC axon (cyan, black lines indicate first TC-to-IN synapse along the TC axon) innervate 96% of the SpS (blue squares) and 93% of StP (magenta squares, IN synapses as green lines) that were also innervated by that TC axon (three fully reconstructed TC axon examples; 100% ExN targets match between IN and TC synapses when only considering StP and SpS within the barrel hollow).

(G) Histogram of TC synapse positions for the cFFI triads, indicating coincident activation of IN and SpS, offset from activation of StP.

(H) TC axon diameters show substantial reduction in the unmyelinated TC axon within L4, making timing effects of synapse sorting plausible (compare Schmidt et al., 2017). Axon diameter was measured at random locations along 3 TC axons (gray lines, average, black, single measurements in inset).

(I) Example cross-sections of TC axon at 44 µm (left) and 122 µm (right) path length showing difference in myelinization and diameter. Scale bars, 100 µm (A–C); 50 µm (D); 1 µm (I).

histograms for individual neurons typically showed a robust spiking response to both the backward (caudal, "on" response) and forward (rostral, "off" response) deflection of the whisker (see Figures 7G and 7H for examples). Average stimulus-evoked AP counts in StP neurons were more twice that of SpS neurons (Figure 7I; response AP counts with spontaneous rate subtracted (median and range): StP 0.597, −0.163 to 2.970, n = 24 neurons, SpS 0.244, −0.127 to 1.444, n = 18 neurons, Wilcoxon rank-sum test p = 0.007), while average spontaneous AP counts were not different (median and range, StP 0.366, 0.277 to 0.283, n = 24 neurons vs. SpS 0.276, 0.154 to 0.315, n = 18 neurons, rank-sum test p = 0.297; Figure S5F). The inter-cell-type difference in evoked APs was found more significant when compared between top 50th percentiles from two groups with ranked responses (median and range, StP 0.885, 0.603 to 2.970, n = 24 neurons vs. SpS 0.471, 0.246 to 1.444, n = 18 neurons, rank-sum

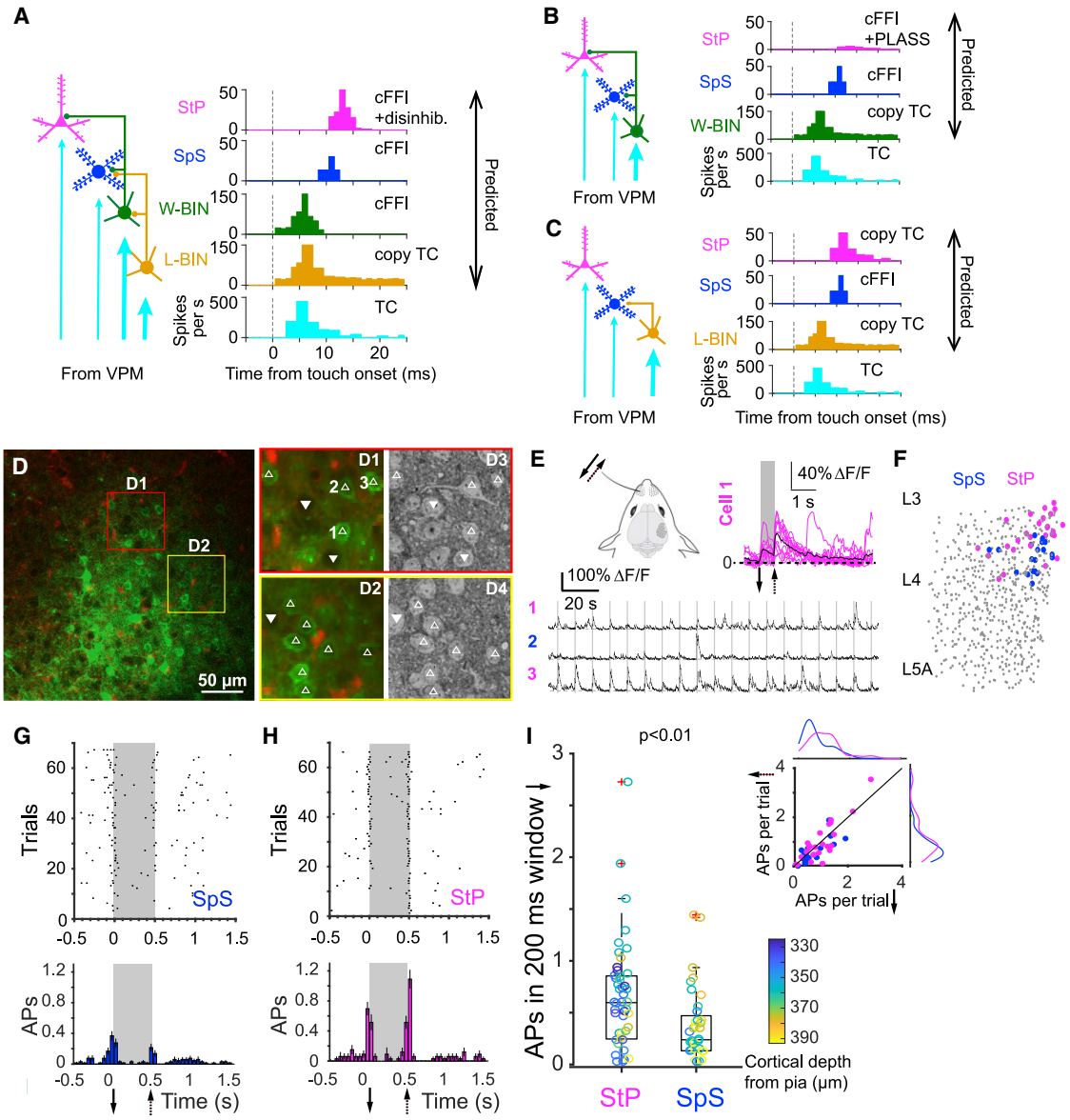

Figure 7. Possible functional effects of TC-driven subtype-specific disinhibitory circuitry in L4

(A) Activation of the entire TC-driven circuitry in L4 would initially yield cFFI onto both SpS and StP, which would be stronger on SpS (two input IN populations). Subsequently, the L-BIN-to-W-BIN inhibitory connectivity could curtail W-BIN activity, thereby relieving StP from cFFI, yielding a stronger StP response.

(B) TC activation of ExNs and exclusive activation of W-BINs would yield cellular feedforward inhibition, effectively increasing activation threshold in ExNs (Yu et al., 2016, 2019) and limiting the time window of activation for SpS and StP. The synaptic offsets in the W-BIN-to-StP pathway could even suppress StP activity (as in Schmidt et al., 2017).

(C) Exclusive TC activation of L-BINs but not W-BINs would yield cFFI for SpS (as in A), but would leave StP without direct thalamus-driven FFI, thus with potentially strong and broad StP activity. (A) would be plausible based on the strong TC clustering for W-BINs, which could allow a selective activation of W-BIN but not L-BIN for sparse or weak thalamic input. Strong thalamic activity could yield setting (C). Note further that instead of impulse response, these circuits could yield differential frequency responses to various temporal patterns of whisker inputs (Arabzadeh et al., 2005; Isett et al., 2018; Jadhav et al., 2009; Wolfe et al., 2008; see discussion).

(D) Neuropil fluorescence (left), two example field of views of high-resolution functional recordings (D1 and D2), and corresponding locations in 3D EM dataset (D3 and D4) with matching somata indicated (labeled somata, triangles; unlabeled somata, inverted triangles; arrows, blood vessels).

(E) Upper left: schematic of recording setup showing direction of whisker deflections for on (solid) and off (dash-line) responses. Stimulus-evoked responses for three example neurons indicated in (D1) showing individual traces (bottom) and average trace of cell 1 (upper right).

(F) Locations of all neuronal somata in the SBEM dataset (gray) with somata of SpS and StP neurons also in the functional dataset shown in blue and magenta, respectively.

(G) Stimulus-triggered AP raster plots for an example SpS neuron (upper) as well as obtained peri-stimulus time histogram (below).

(H) Stimulus-triggered AP raster plots for an example StP neuron (upper) as well as obtained peri-stimulus time histogram (below).

(legend continued on next page)

test $p < 0.001$). In addition, response probability was more than 1.5-fold larger for StP than for SpS neurons (response probability [median and range]: StP, 0.722, 0.076 to 1, n = 24 neurons, SpS 0.467, 0.022 to 0.949, n = 18 neurons, Wilcoxon rank-sum test $p = 0.003$). This strong difference in stimulus-evoked activity was found even though the SpS and StP neurons in our functionally recorded sample were all located in upper L4, thus with only moderate displacement of the cell types along the cortical axis (average displacement, 16.04 ± 24.40 μm, n = 33; maximal displacement, 68 μm).

DISCUSSION

Our analysis of the thalamus-driven inhibitory circuitry in cortical L4 revealed (1) highly specific TC innervation of about 15% of INs in the barrel yielding a clear distinction of TC-INs. (2) All TC-INs have a barrel-restricted axonal projection (synaptic output). (3) TC-INs fall into two classes based on their innervation of spiny stellate vs. star pyramidal cells, implemented via the strong layering of these target cells within L4. (4) Among the TC-INs, a directed disinhibitory circuit exists from L-BINs to W-BINs. (5) The thus defined IN types differ in the strength and degree of clustering of the TC synaptic input they receive. (6) Thalamus-driven FFI circuitry is configured at cellular precision (cFFI) with sorted synaptic outputs along TC axons.

Together, these findings describe a highly precise thalamus-driven inhibitory circuitry that would be capable of creating differential temporal windows for activation of the subtypes of excitatory neurons within L4, possibly allowing for differential representation of sensory stimuli of varying temporal structure.

Connectomic definition of IN types

We used exclusively connectomic information for the distinction of types of INs in L4: strong TC innervation and synaptic target preference for ExN subtypes for the initial IN type definition; and then we found further connectomic specializations of these IN subtypes in their directed disinhibitory synaptic connectivity and strength and clustering of TC input. It was notable that these connectomic differences were multi-fold: 6-fold stronger TC innervation (Figure 2F), 3.5-fold difference in ExN targeting (Figure 3C), 10-fold bias in disinhibitory connectivity (Figure 4C), 1.7-fold difference in unitary TC input synapse number (Figure 3D), and 2.2-fold difference in TC clustering (Figure 3F). Such clear connectomic patterns may be promising for approaching the still debated field of IN type definition (Ascoli et al., 2008; Yuste et al., 2020) from a connectomic perspective (as exemplified before in the retina; Helmstaedter et al., 2013).

Relation to somatostatin IN types

Recent work (Yu et al., 2019) has described the differential TC activation of subtypes of INs identified via their protein expression (parvalbumin [PV] vs. somatostatin [SST] and vasointestinal peptide [VIP]; Pfeffer et al., 2013; Rudy et al., 2011; Scala et al., 2019; Taniguchi et al., 2011; Tremblay et al., 2016). In these data, disinhibition is implied to be provided by SST and VIP INs, while PV-positive INs are the only INs to receive short-latency TC activation (Yu et al., 2019). Our data indicate that even subtypes of locally projecting soma-targeting INs (likely identified with PV-positive INs) differentially provide disinhibition within the barrel (Figure 4). Since SST-INs are described as preferentially dendrite targeting (Pfeffer et al., 2013; Scala et al., 2019; Williams and Holtmaat, 2019), it is unlikely that the L-BINs correspond to these IN subtypes. Rather, the identification by the classical IN markers may not be sufficient in L4. Recent data have proposed that SST-INs have unconventional morphology in S1 (Scala et al., 2019; Zhou et al., 2020). It has to be determined whether the circuits we found are related to the conventional expression markers widely employed (see also Koelbl et al., 2015 for the [lack of] relation between morphology, markers, and electrophysiology in L4, and Table S1 for a tentative comparison of our INs to published data).

Sublayers within cortical layer 4 in other species

In primates, cats, and higher mammals (Braak, 1976; Clark, 1925; Collins et al., 2005; Hassler and Wagner, 1965; Kaas et al., 1972; Lund, 1973; Otsuka and Hassler, 1962; Wong and Kaas, 2008, 2009, 2010), cortical L4 in primary sensory areas has been subdivided since the initial histological analyses (Brodmann, 1909; Ramón y Cajal, 1899). These subdivisions were based on overall histoarchitectonic differences in cell body density (Brodmann, 1909; Campbell et al., 1905; Garey and Harris, 1971; Lewis and Ferrier, 1880; Ramón y Cajal, 1899; Valverde, 1977; von Bonin, 1942). In macaque and cat, the observation of more pyramidal cells toward L3 gave rise to a dispute of where to define the upper border of L4 (Garey and Harris, 1971). A subdivision of L4 by excitatory cell type was not clearly accepted in these species. For rodents, a subdivision of L4 has not been described, and even less one related to the types of excitatory cells; yet, with the benefit of hindsight, some evidence can be found (Simons and Woolsey, 1984). Since the stacked positioning of neurons that we find (Figure 1) is only clearly visible within the barrel, but not in the septa, and since it occurs on spatial scales of less than 200 μm, it may have evaded light-microscopy-based circuit analysis.

cFFI in mammalian cortex

While feedforward inhibition as a key wiring principle has been identified in many mammalian circuits in the cortex (Alger and Nicoll, 1982; Bruno and Simons, 2002; Buzsáki, 1984; Cruikshank et al., 2007; Duguid et al., 2015; Isaacson and Scanziani, 2011; Kanichay and Silver, 2008; Kloc and Maffei, 2014; Mittmann et al., 2005; Pouille and Scanziani, 2001), it was not possible to distinguish between population-level or cellular-precision FFI. 3D EM has allowed the systematic investigation of this, and so far it has identified cFFI as a prevailing wiring principle intracortically in supragranular layers (Schmidt et al., 2017)

(l) Boxplots of average AP count for all stimulus-evoked responses (both "on" and "off" responses, spontaneous rate subtracked) for StP and SpS groups. Open circles represent individual neurons, color coded by the cortical depth of its soma from the pia. Box is median and 25th and 75th percentiles; whiskers show data range. Inset: average stimulus-evoked "on" and "off" AP response per trial (in 200-ms window around stimulus onset of offset) for all StP (magenta) and SpS (blue) neurons. Smoothed histograms above and right represent the distributions of responses to caudal and rostral movement respectively.

and for TC input to cortex (this study, Figure 3). In combination with axonal synapse sorting (PLASS; Schmidt et al., 2017), such circuits can theoretically very precisely control the propagation of excitatory activity (Schmidt et al., 2017). While synaptic placement as a means for temporally precise neuronal activity has been long known in non-mammalian species (Carr and Konishi, 1990; Kornfeld et al., 2017), the degree of precision in mammalian cortical tissue is surprising. Whether AP conduction in TC axons is slow enough to allow full excitatory suppression (Schmidt et al., 2017) or rather a narrowed window of postsynaptic activation will have to be investigated. The level of circuit precision observed here indicates that very detailed studies are required for an analysis of the capacity of these circuits in mammals.

Circuit effects on temporal patterns of sensory stimuli

The surprising circuit-level differences in the thalamic feedforward convergence onto SpS vs. StP neurons (Figure 7) could allow for differential representation of sensory stimuli with different temporal structure. In particular upon strong VPM activation, when both W-BINs and L-BINs are predicted to be active (Figure 7C), SpS cells are predicted to respond with higher temporal fidelity to TC input, while StPs are predicted to have a delayed response governed by the disinhibitory delay (the time it takes to inhibit W-BINs by L-BINs), which then however could be much stronger than in SpS. In principle, such a configuration could imply a high-vs. low-pass filtering of sensory inputs. One can speculate that this could correspond to the representation of smooth (high temporal input frequency) vs. rougher (low temporal frequencies) surfaces via the principal whisker (Arabzadeh et al., 2005; Carvell and Simons, 1990; Isett et al., 2018; Jadhav et al., 2009; Park et al., 2019; Wu et al., 2013). Key caveats to this interpretation are whether the L-BIN connection to W-BINs is strong enough to fully suppress W-BIN activity even under concomitant thalamic input, and whether other inhibitory sources may become important already within the first 10 ms after the sensory stimulus.

Limitations of the study

We have provided a connectomic description of the thalamus-driven inhibitory L4 circuits in mammalian sensory cortex. These data, however, did not provide the structure of the excitatory intracortical networks, which will be essential for determining whether the level of precision found here in synaptic and cellular architecture is an overarching principle of mammalian cortex. For this, larger-volume 3D EM techniques will be crucial that allow acquiring 0.5- to 1-mm-scale volumes at high EM resolution, which we were not able to obtain using the SBEM technique. Functionally, the observed high-precision synaptic circuitry indicates that sub-millisecond temporal precision in synaptic transmission and action potential generation may be relevant in these circuits. Our functional recordings were not designed to observe such high temporal precision, yet.

STAR★METHODS

Detailed methods are provided in the online version of this paper and include the following:

SUPPLEMENTAL INFORMATION

Supplemental information can be found online at https://doi.org/10.1016/j.celrep.2022.111476.

ACKNOWLEDGMENTS

We thank A. Motta for comments on an earlier version of the manuscript, I. Wolf for staining support, S. Babl, L. Bezzenberger, R. Jakoby, R. Kneiβl, and M. Kronawitter for annotator training and task management, H. Wissler for tracer management and support with figure generation, and A. Kessler, A. Brandt, A.J. Lopez, A. Strubel, A. Weyh, A. Kolbinger, A. Fantur, A.K. Spohner, A. Rix, A. Possmayer, A. Bamberg, A. Machel, A. Al-Shaboti, B. Kuhl, B. Heftrich, B.L. Stiehl, C. Lossnitzer, C.A. Sandhof, C. Arras, C. Sabatelli, C. Schumm, C. Kurz, D. Beyer, D. Baltissen, D. Greco, D. Celik, D. Kurt, D. Acay, D.J. Scheliu, E. Laube, F. Gohl, F. Sahin, F.Y. Basoeki, F. Krämer, H. Charif, H. Hees, I. Meindl, I. Stasiuk, I. Metz, J. Winkelmeier, J. Hartel, J. Meyer, J.E. Martínez, J. Knauer, J. Depnering, J. Heller, J. Kubat, J. Buss, K. Kramer, K. Strahler, K. Trares, K. Desch, K. Lust, L. Buxmann, L. Matzner, L. Kirchner, L. Praeve, L. Kreppner, L. Schütz, L. Bezzenberger, L. Hartwig, L. Lutz, L. Burchartz, M. Aly, M. Werr, M. Dell, M. Nonnenbroich, M. Harwardt, M. Mittag, M. Grootthuis, M. Präve, M. Karabel, M. Weber, N. Cipta, N. Zeitzschel, N. Aydin, N. Berghaus, N. Böffinger, O. Ilea, P. König, P. Remmele, P. Müller, P. Werner, R. Gebauer, R. Hülse, R. Thieleking, S. Reichel, S. Mehlmann, S.T. Stahl, S. Umbach, S. Wehrheim, S. Bohne, S. Reibeling, S. Lerchl, T. Köcke, T. Ernst, T. Decker, T. Engelmann, T. Winkelmeier, T. Hörmann, T. Reimann, V. Kalbert, V. Pantle, V. Robl, V. Gosch, V. Dienst, W. Pfohl, H. Wang, Y. Lu, H. Sheng, Y. Qi, and S. Wang for neuron reconstructions. All work was funded by the Max Planck Society.

AUTHOR CONTRIBUTIONS

M.H. conceived, initiated, and supervised the study; Y.H. conducted EM experiments with contributions by P.L. using 3D EM methodology contributed by K.M.B.; Y.H., S.L., and M.H. analyzed structural data; J.K. supervised, and Y.H., V.P., K.M.V., and D.L.W. conducted functional recordings and analysis. Y.H., S.L., and M.H. wrote the paper with contributions by all authors.

DECLARATION OF INTERESTS

P.L. is an employee of Databricks, Inc. K.M.B. is an employee of Palindromics, Inc. Current affiliation (K.M.B.): Department of Physics, The University of Illinois at Chicago.

Received: January 28, 2022
Revised: July 29, 2022
Accepted: September 19, 2022
Published: October 11, 2022

REFERENCES

Agmon, A., and Connors, B.W. (1991). Thalamocortical responses of mouse somatosensory (barrel) cortexin vitro. Neuroscience *41*, 365–379.

Ahmed, B., Anderson, J.C., Douglas, R.J., Martin, K.A., and Nelson, J.C. (1994). Polyneuronal innervation of spiny stellate neurons in cat visual cortex. J. Comp. Neurol. *341*, 39–49.

Ahmed, B., Anderson, J.C., Martin, K.A., and Nelson, J.C. (1997). Map of the synapses onto layer 4 basket cells of the primary visual cortex of the cat. J. Comp. Neurol. *380*, 230–242.

Alger, B.E., and Nicoll, R.A. (1982). Feed-forward dendritic inhibition in rat hippocampal pyramidal cells studied in vitro. J. Physiol. *328*, 105–123.

Arabzadeh, E., Zorzin, E., and Diamond, M.E. (2005). Neuronal encoding of texture in the whisker sensory pathway. PLoS Biol. *3*, e17.

Ascoli, G.A., Alonso-Nanclares, L., Barrionuevo, G., Burkhalter, A., Cauli, B., Fairén, A., Fishell, G., Freund, T.F., Gardner, E.P., Helmstaedter, M., et al.; Petilla Interneuron Nomenclature Group (2008). Petilla terminology: nomenclature of features of GABAergic interneurons of the cerebral cortex. Nat. Rev. Neurosci. *9*, 557–568.

Bagnall, M.W., Hull, C., Bushong, E.A., Ellisman, M.H., and Scanziani, M. (2011). Multiple clusters of Release sites formed by individual thalamic afferents onto cortical interneurons ensure reliable transmission. Neuron *71*, 180–194.

Bastian Bechtold, P.F., Seamusholden, and Gorur-Shandilya., S. (2016). Bastibe/violinplot-matlab: a good starting point (v0.1). Zenodo. https://doi.org/10.5281/zenodo.4559847.

Bay, H., Ess, A., Tuytelaars, T., and Van Gool, L. (2008). Speeded-up robust features (SURF). Comput. Vis. Image Understand. *110*, 346–359.

Beierlein, M., Gibson, J.R., and Connors, B.W. (2000). A network of electrically coupled interneurons drives synchronized inhibition in neocortex. Nat. Neurosci. *3*, 904–910.

Beierlein, M., Gibson, J.R., and Connors, B.W. (2003). Two dynamically distinct inhibitory networks in layer 4 of the neocortex. J. Neurophysiol. *90*, 2987–3000.

Bereshpolova, Y., Hei, X., Alonso, J.-M., and Swadlow, H.A. (2020). Three rules govern thalamocortical connectivity of fast-spike inhibitory interneurons in the visual cortex. Elife *9*, e60102.

Boergens, K.M., Berning, M., Bocklisch, T., Bräunlein, D., Drawitsch, F., Frohnhofen, J., Herold, T., Otto, P., Rzepka, N., Werkmeister, T., et al. (2017). webKnossos: efficient online 3D data annotation for connectomics. Nat. Methods *14*, 691–694.

Bopp, R., Holler-Rickauer, S., Martin, K.A.C., and Schuhknecht, G.F.P. (2017). An ultrastructural study of the thalamic input to layer 4 of primary motor and primary somatosensory cortex in the mouse. J. Neurosci. *37*, 2435–2448.

Braak, H. (1976). On the striate area of the human isocortex. A golgi- and pigmentarchitectonic study. J. Comp. Neurol. *166*, 341–364.

Brecht, M., and Sakmann, B. (2002). Dynamic representation of whisker deflection by synaptic potentials in spiny stellate and pyramidal cells in the barrels and septa of layer 4 rat somatosensory cortex. J. Physiol. *543*, 49–70.

Brodmann, K. (1909). Vergleichende Lokalisationslehre der Grosshirnrinde in ihren Prinzipien dargestellt auf Grund des Zellenbaues (Johann Ambrosius Barth).

Bruno, R.M., and Sakmann, B. (2006). Cortex is driven by weak but synchronously active thalamocortical synapses. Science *312*, 1622–1627.

Bruno, R.M., and Simons, D.J. (2002). Feedforward mechanisms of excitatory and inhibitory cortical receptive fields. J. Neurosci. *22*, 10966–10975.

Buzsáki, G. (1984). Feed-forward inhibition in the hippocampal formation. Prog. Neurobiol. *22*, 131–153.

Campbell, A.W., Schlesinger, E.B., and Riley, H.A. (1905). Histological Studies on the Localisation of Cerebral Function (University Press).

Carr, C.E., and Konishi, M. (1990). A circuit for detection of interaural time differences in the brain stem of the barn owl. J. Neurosci. *10*, 3227–3246.

Carvell, G.E., and Simons, D.J. (1990). Biometric analyses of vibrissal tactile discrimination in the rat. J. Neurosci. *10*, 2638–2648.

Clark, W.E. (1925). The visual cortex of primates. J. Anat. *59*, 350–357.

Collins, C.E., Hendrickson, A., and Kaas, J.H. (2005). Overview of the visual system of tarsius. Anat. Rec. A Discov. Mol. Cell. Evol. Biol. *287*, 1013–1025.

Connors, B.W. (2017). Synchrony and so much more: diverse roles for electrical synapses in neural circuits. Dev. Neurobiol. *77*, 610–624.

Cruikshank, S.J., Lewis, T.J., and Connors, B.W. (2007). Synaptic basis for intense thalamocortical activation of feedforward inhibitory cells in neocortex. Nat. Neurosci. *10*, 462–468.

de Kock, C.P.J., Bruno, R.M., Spors, H., and Sakmann, B. (2007). Layer- and cell-type-specific suprathreshold stimulus representation in rat primary somatosensory cortex. J. Physiol. *581*, 139–154.

Denk, W., and Horstmann, H. (2004). Serial block-face scanning electron microscopy to reconstruct three-dimensional tissue nanostructure. PLoS Biol. *2*, e329.

Denk, W., Strickler, J.H., and Webb, W.W. (1990). Two-photon laser scanning fluorescence microscopy. Science *248*, 73–76.

Duguid, I., Branco, T., Chadderton, P., Arlt, C., Powell, K., and Häusser, M. (2015). Control of cerebellar granule cell output by sensory-evoked Golgi cell inhibition. Proc. Natl. Acad. Sci. USA *112*, 13099–13104.

Egger, V., Nevian, T., and Bruno, R.M. (2008). Subcolumnar dendritic and axonal organization of spiny stellate and star pyramid neurons within a barrel in rat somatosensory cortex. Cereb. Cortex *18*, 876–889.

Elston, G.N., Pow, D.V., and Calford, M.B. (1997). Neuronal composition and morphology in layer IV of two vibrissal barrel subfields of rat cortex. Cereb. Cortex *7*, 422–431.

Feldmeyer, D., Egger, V., Lübke, J., and Sakmann, B. (1999). Reliable synaptic connections between pairs of excitatory layer 4 neurones within a single 'barrel' of developing rat somatosensory cortex. J. Physiol. *521* (*Pt 1*), 169–190.

Gabernet, L., Jadhav, S.P., Feldman, D.E., Carandini, M., and Scanziani, M. (2005). Somatosensory integration controlled by dynamic thalamocortical feed-forward inhibition. Neuron *48*, 315–327.

Gainey, M.A., Aman, J.W., and Feldman, D.E. (2018). Rapid disinhibition by adjustment of PV intrinsic excitability during whisker map plasticity in mouse S1. J. Neurosci. *38*, 4749–4761.

Galarreta, M., and Hestrin, S. (1999). A network of fast-spiking cells in the neocortex connected by electrical synapses. Nature *402*, 72–75.

Garey, L.J., and Harris, G.W. (1971). A light and electron microscopic study of the visual cortex of the cat and monkey. Proc. R. Soc. Lond. B Biol. Sci. *179*, 21–40.

Gibson, J.R., Beierlein, M., and Connors, B.W. (1999). Two networks of electrically coupled inhibitory neurons in neocortex. Nature *402*, 75–79.

Greenberg, D.S., and Kerr, J.N.D. (2009). Automated correction of fast motion artifacts for two-photon imaging of awake animals. J. Neurosci. Methods *176*, 1–15.

Greenberg, D.S., Wallace, D.J., Voit, K.-M., Wuertenberger, S., Czubayko, U., Monsees, A., Handa, T., Vogelstein, J.T., Seifert, R., Groemping, Y., et al. (2018). Accurate action potential inference from a calcium sensor protein through biophysical modeling. Preprint at bioRxiv. https://doi.org/10.1101/479055.

Gutnisky, D.A., Yu, J., Hires, S.A., To, M.S., Bale, M.R., Svoboda, K., and Golomb, D. (2017). Mechanisms underlying a thalamocortical transformation during active tactile sensation. PLoS Comput. Biol. *13*, e1005576.

Hassler, R., and Wagner, A. (1965). Experimentelle und morphologische Befunde über die vierfache corticale Projektion des visuellen Systems. Paper presented at: Eighth International Congress on Neurology.

Hatch, R.J., Mendis, G.D.C., Kaila, K., Reid, C.A., and Petrou, S. (2017). Gap junctions link regular-spiking and fast-spiking interneurons in layer 5 somatosensory cortex. Front. Cell. Neurosci. *11*, 204.

Helmstaedter, M., Briggman, K.L., Turaga, S.C., Jain, V., Seung, H.S., and Denk, W. (2013). Connectomic reconstruction of the inner plexiform layer in the mouse retina. Nature *500*, 168–174.

Hestrin, S., and Galarreta, M. (2005). Electrical synapses define networks of neocortical GABAergic neurons. Trends Neurosci. *28*, 304–309.

Horn, B.K.P. (1987). Closed-form solution of absolute orientation using unit quaternions. J. Opt. Soc. Am. A *4*, 629–642.

House, D.R.C., Elstrott, J., Koh, E., Chung, J., and Feldman, D.E. (2011). Parallel regulation of feedforward inhibition and excitation during whisker map plasticity. Neuron *72*, 819–831.

Hua, Y., Laserstein, P., and Helmstaedter, M. (2015). Large-volume en-bloc staining for electron microscopy-based connectomics. Nat. Commun. *6*, 7923.

Hubel, D.H., and Wiesel, T.N. (1962). Receptive fields, binocular interaction and functional architecture in the cat's visual cortex. J. Physiol. *160*, 106–154.

Isaacson, J.S., and Scanziani, M. (2011). How inhibition shapes cortical activity. Neuron *72*, 231–243.

Isett, B.R., Feasel, S.H., Lane, M.A., and Feldman, D.E. (2018). Slip-based coding of local shape and texture in mouse S1. Neuron *97*, 418–433.e5.

Jacobson, M. (2022). Absolute Orientation - Horn's Method. MATLAB Central File Exchange. https://www.mathworks.com/matlabcentral/fileexchange/26186-absolute-orientation-horn-s-method. (Accessed 31 August 2022).

Jadhav, S.P., Wolfe, J., and Feldman, D.E. (2009). Sparse temporal coding of elementary tactile features during active whisker sensation. Nat. Neurosci. *12*, 792–800.

Kaas, J.H., Hall, W.C., and Diamond, I.T. (1972). Visual cortex of the grey squirrel (Sciurus carolinensis): architectonic subdivisions and connections from the visual thalamus. J. Comp. Neurol. *145*, 273–305.

Kanichay, R.T., and Silver, R.A. (2008). Synaptic and cellular properties of the feedforward inhibitory circuit within the input layer of the cerebellar cortex. J. Neurosci. *28*, 8955–8967.

Kanold, P.O., Kara, P., Reid, R.C., and Shatz, C.J. (2003). Role of subplate neurons in functional maturation of visual cortical columns. Science *301*, 521–525.

Kara, P., Pezaris, J.S., Yurgenson, S., and Reid, R.C. (2002). The spatial receptive field of thalamic inputs to single cortical simple cells revealed by the interaction of visual and electrical stimulation. Proc. Natl. Acad. Sci. USA *99*, 16261–16266.

Karimi, A., Odenthal, J., Drawitsch, F., Boergens, K.M., and Helmstaedter, M. (2020). Cell-type specific innervation of cortical pyramidal cells at their apical dendrites. Elife *9*, e46876.

Karnani, M.M., Jackson, J., Ayzenshtat, I., Hamzehei Sichani, A., Manoocheri, K., Kim, S., and Yuste, R. (2016). Opening holes in the blanket of inhibition: localized lateral disinhibition by VIP interneurons. J. Neurosci. *36*, 3471–3480.

Kloc, M., and Maffei, A. (2014). Target-specific properties of thalamocortical synapses onto layer 4 of mouse primary visual cortex. J. Neurosci. *34*, 15455–15465.

Koelbl, C., Helmstaedter, M., Lübke, J., and Feldmeyer, D. (2015). A barrel-related interneuron in layer 4 of rat somatosensory cortex with a high intrabarrel connectivity. Cereb. Cortex *25*, 713–725.

Kornfeld, J., Benezra, S.E., Narayanan, R.T., Svara, F., Egger, R., Oberlaender, M., Denk, W., and Long, M.A. (2017). EM connectomics reveals axonal target variation in a sequence-generating network. Elife *6*, e24364.

Lee, S., Kruglikov, I., Huang, Z.J., Fishell, G., and Rudy, B. (2013). A disinhibitory circuit mediates motor integration in the somatosensory cortex. Nat. Neurosci. *16*, 1662–1670.

LeVay, S. (1973). Synaptic patterns in the visual cortex of the cat and monkey. Electron microscopy of Golgi Preparations. J. Comp. Neurol. *150*, 53–85.

Lewis, W.B., and Ferrier, D. (1880). III. Researches on the comparative structure of the cortex cerebri. Phil. Trans. Roy. Soc. Lond. *171*, 35–64.

Lorente De No, R. (1938). Cerebral cortex : architecture, intracortical connections, motor projections. Physiol. Nervous Syst., 288–313.

Lübke, J., Egger, V., Sakmann, B., and Feldmeyer, D. (2000). Columnar organization of dendrites and axons of single and synaptically coupled excitatory spiny neurons in layer 4 of the rat barrel cortex. J. Neurosci. *20*, 5300–5311.

Lübke, J., Roth, A., Feldmeyer, D., and Sakmann, B. (2003). Morphometric analysis of the columnar innervation domain of neurons connecting layer 4 and layer 2/3 of juvenile rat barrel cortex. Cereb. Cortex *13*, 1051–1063.

Lund, J.S. (1973). Organization of neurons in the visual cortex, area 17, of the monkey (Macaca mulatta). J. Comp. Neurol. *147*, 455–496.

Martinez, L.M., Wang, Q., Reid, R.C., Pillai, C., Alonso, J.-M., Sommer, F.T., and Hirsch, J.A. (2005). Receptive field structure varies with layer in the primary visual cortex. Nat. Neurosci. *8*, 372–379.

McCormick, D.A., Connors, B.W., Lighthall, J.W., and Prince, D.A. (1985). Comparative electrophysiology of pyramidal and sparsely spiny stellate neurons of the neocortex. J. Neurophysiol. *54*, 782–806.

Mittmann, W., Koch, U., and Häusser, M. (2005). Feed-forward inhibition shapes the spike output of cerebellar Purkinje cells. J. Physiol. *563*, 369–378.

Motta, A., Berning, M., Boergens, K.M., Staffler, B., Beining, M., Loomba, S., Hennig, P., Wissler, H., and Helmstaedter, M. (2019). Dense connectomic reconstruction in layer 4 of the somatosensory cortex. Science *366*, eaay3134.

Oberlaender, M., Ramirez, A., and Bruno, R.M. (2012). Sensory experience restructures thalamocortical axons during adulthood. Neuron *74*, 648–655.

Otsuka, R., and Hassler, R. (1962). Über Aufbau und Gliederung der corticalen Sehsphäre bei der Katze. Arch. Psychiatr. Nervenkr. Z. Gesamte Neurol. Psychiatr. *203*, 212–234.

Park, J., Rodgers, C., Hong, Y.K., Dahan, J., and Bruno, R. (2019). Primary somatosensory cortex is essential for texture discrimination but not object detection in mice. IBRO Rep. *6*, S550.

Pavao, R. (2022). Optimization of Parameters of the Sigmoid Function. MATLAB Central File Exchange. https://www.mathworks.com/matlabcentral/fileexchange/42641-sigm_fit. (Accessed 31 August 2022).

Pernelle, G., Nicola, W., and Clopath, C. (2018). Gap junction plasticity as a mechanism to regulate network-wide oscillations. PLoS Comput. Biol. *14*, e1006025.

Pfeffer, C.K., Xue, M., He, M., Huang, Z.J., and Scanziani, M. (2013). Inhibition of inhibition in visual cortex: the logic of connections between molecularly distinct interneurons. Nat. Neurosci. *16*, 1068–1076.

Porter, J.T., Johnson, C.K., and Agmon, A. (2001). Diverse types of interneurons generate thalamus-evoked feedforward inhibition in the mouse barrel cortex. J. Neurosci. *21*, 2699–2710.

Pouille, F., and Scanziani, M. (2001). Enforcement of temporal fidelity in pyramidal cells by somatic feed-forward inhibition. Science *293*, 1159–1163.

Ramachandra, V., Pawlak, V., Wallace, D.J., and Kerr, J.N.D. (2020). Impact of visual callosal pathway is dependent upon ipsilateral thalamus. Nat. Commun. *11*, 1889.

Ramón y Cajal, S. (1899). Estudios sobre la corteza cerebral humana. Corteza visual. Rev. Trim. Microgr. *4*, 1–63.

Rikhye, R.V., Yildirim, M., Hu, M., Breton-Provencher, V., and Sur, M. (2021). Reliable sensory processing in mouse visual cortex through cooperative interactions between somatostatin and parvalbumin interneurons. J. Neurosci. *41*, 8761–8778.

Rudy, B., Fishell, G., Lee, S., and Hjerling-Leffler, J. (2011). Three groups of interneurons account for nearly 100% of neocortical GABAergic neurons. Dev. Neurobiol. *71*, 45–61.

Scala, F., Kobak, D., Shan, S., Bernaerts, Y., Laturnus, S., Cadwell, C.R., Hartmanis, L., Froudarakis, E., Castro, J.R., Tan, Z.H., et al. (2019). Layer 4 of mouse neocortex differs in cell types and circuit organization between sensory areas. Nat. Commun. *10*, 5075.

Schmidt, H., Gour, A., Straehle, J., Boergens, K.M., Brecht, M., and Helmstaedter, M. (2017). Axonal synapse sorting in medial entorhinal cortex. Nature *549*, 469–475.

Schubert, D., Kötter, R., Zilles, K., Luhmann, H.J., and Staiger, J.F. (2003). Cell type-specific circuits of cortical layer IV spiny neurons. J. Neurosci. *23*, 2961–2970.

Simons, D.J., and Woolsey, T.A. (1984). Morphology of Golgi-Cox-impregnated barrel neurons in rat SmI cortex. J. Comp. Neurol. *230*, 119–132.

Staffler, B., Berning, M., Boergens, K.M., Gour, A., Smagt, P.v.d., and Helmstaedter, M. (2017). SynEM, automated synapse detection for connectomics. Elife *6*, e26414.

Staiger, J.F., Flagmeyer, I., Schubert, D., Zilles, K., Kötter, R., and Luhmann, H.J. (2004). Functional diversity of layer IV spiny neurons in rat somatosensory cortex: quantitative morphology of electrophysiologically characterized and biocytin labeled cells. Cereb. Cortex *14*, 690–701.

Staiger, J.F., Zuschratter, W., Luhmann, H.J., and Schubert, D. (2009). Local circuits targeting parvalbumin-containing interneurons in layer IV of rat barrel cortex. Brain Struct. Funct. *214*, 1–13.

Stratford, K.J., Tarczy-Hornoch, K., Martin, K.A., Bannister, N.J., and Jack, J.J. (1996). Excitatory synaptic inputs to spiny stellate cells in cat visual cortex. Nature *382*, 258–261.

Sun, Q.-Q., Huguenard, J.R., and Prince, D.A. (2006). Barrel cortex microcircuits: thalamocortical feedforward inhibition in spiny stellate cells is mediated by a small number of fast-spiking interneurons. J. Neurosci. *26*, 1219–1230.

Swadlow, H.A. (2003). Fast-spike interneurons and feedforward inhibition in awake sensory neocortex. Cereb. Cortex *13*, 25–32.

Taniguchi, H., He, M., Wu, P., Kim, S., Paik, R., Sugino, K., Kvitsiani, D., Kvitsani, D., Fu, Y., Lu, J., et al. (2011). A resource of cre driver lines for genetic targeting of GABAergic neurons in cerebral cortex. Neuron *71*, 995–1013.

Temereanca, S., and Simons, D.J. (2004). Functional topography of corticothalamic feedback enhances thalamic spatial response tuning in the somatosensory whisker/barrel system. Neuron *41*, 639–651.

Torii, M., and Levitt, P. (2005). Dissociation of corticothalamic and thalamocortical axon targeting by an EphA7-mediated mechanism. Neuron *48*, 563–575.

Tremblay, R., Lee, S., and Rudy, B. (2016). GABAergic interneurons in the neocortex: from cellular properties to circuits. Neuron *91*, 260–292.

Valverde, F. (1977). Lamination of the striate cortex. J. Neurocytol. *6*, 483–484.

von Bonin, G. (1942). The striate area of primates. J. Comp. Neurol. *77*, 405–429.

White, E.L. (1978). Identified neurons in mouse smi cortex which are postsynaptic to thalamocortical axon terminals: a combined golgi-electron microscopic and degeneration study. J. Comp. Neurol. *181*, 627–661.

Williams, L.E., and Holtmaat, A. (2019). Higher-order thalamocortical inputs gate synaptic long-term potentiation via disinhibition. Neuron *101*, 91–102.e4.

Wolfe, J., Hill, D.N., Pahlavan, S., Drew, P.J., Kleinfeld, D., and Feldman, D.E. (2008). Texture coding in the rat whisker system: slip-stick versus differential resonance. PLoS Biol. *6*, e215.

Wong, P., and Kaas, J.H. (2008). Architectonic subdivisions of neocortex in the gray squirrel (Sciurus carolinensis). Anat. Rec. *291*, 1301–1333.

Wong, P., and Kaas, J.H. (2009). Architectonic subdivisions of neocortex in the tree shrew (Tupaia belangeri). Anat. Rec. *292*, 994–1027.

Wong, P., and Kaas, J.H. (2010). Architectonic subdivisions of neocortex in the Galago (Otolemur garnetti). Anat. Rec. *293*, 1033–1069.

Woolsey, T.A., Dierker, M.L., and Wann, D.F. (1975). Mouse SmI cortex: qualitative and quantitative classification of golgi-impregnated barrel neurons. Proc. Natl. Acad. Sci. USA *72*, 2165–2169.

Woolsey, T.A., and Van der Loos, H. (1970). The structural organization of layer IV in the somatosensory region (SI) of mouse cerebral cortex. The description of a cortical field composed of discrete cytoarchitectonic units. Brain Res. *17*, 205–242.

Wu, H.-P.P., Ioffe, J.C., Iverson, M.M., Boon, J.M., and Dyck, R.H. (2013). Novel, whisker-dependent texture discrimination task for mice. Behav. Brain Res. *237*, 238–242.

Xu, H., Jeong, H.-Y., Tremblay, R., and Rudy, B. (2013). Neocortical somatostatin-expressing GABAergic interneurons disinhibit the thalamorecipient layer 4. Neuron *77*, 155–167.

Yeatman, J.D., Dougherty, R.F., Myall, N.J., Wandell, B.A., and Feldman, H.M. (2012). Tract profiles of white matter properties: automating fiber-tract quantification. PLoS One *7*, e49790.

Yu, J., Gutnisky, D.A., Hires, S.A., and Svoboda, K. (2016). Layer 4 fast-spiking interneurons filter thalamocortical signals during active somatosensation. Nat. Neurosci. *19*, 1647–1657.

Yu, J., Hu, H., Agmon, A., and Svoboda, K. (2019). Recruitment of GABAergic interneurons in the barrel cortex during active tactile behavior. Neuron *104*, 412–427.e4.

Yuste, R., Hawrylycz, M., Aalling, N., Aguilar-Valles, A., Arendt, D., Armañanzas, R., Ascoli, G.A., Bielza, C., Bokharaie, V., Bergmann, T.B., et al. (2020). A community-based transcriptomics classification and nomenclature of neocortical cell types. Nat. Neurosci. *23*, 1456–1468.

Zhou, X., Mansori, I., Fischer, T., Witte, M., and Staiger, J.F. (2020). Characterizing the morphology of somatostatin-expressing interneurons and their synaptic innervation pattern in the barrel cortex of the GFP-expressing inhibitory neurons mouse. J. Comp. Neurol. *528*, 244–260.

STAR★METHODS

KEY RESOURCES TABLE

REAGENT or RESOURCE	SOURCE	IDENTIFIER
Bacterial and virus strains		
pAAV.CAG.Flex.GCaMP6s.WPRE.SV40	Addgene	#100845-AAV1
Deposited data		
Dual-color 2-photon z-stack	This paper	https://wklink.org/2196
Interneuron dendrites with all input synapses	This paper	https://wklink.org/8100
Connectome consisting of interneuron and thalamocortical axons as well as interneuron and excitatory neuron dendrites	This paper	https://wklink.org/6197
Interneuron-to-interneuron dendro-dendritic contactome	This paper	https://wklink.org/8200
All interneuron (n = 58) tracings in motortile 4 of SBEM data	This paper	https://wklink.org/8500
Experimental models: Organisms/strains		
Mouse (B6;C3-Tg(Scnn1a-cre)3Aibs/J)	Jackson Laboratory	009613
Software and algorithms		
Code used for analysis	This paper	https://doi.org/10.5281/zenodo.7080629
webKnossos	Boergens et al., 2017	https://webknossos.org
Action potential inference algorithm	Greenberg et al., 2018	https://doi.org/10.1101/479055
MATLAB and Statistics Toolbox	MathWorks, Inc	Release 2021a
Absolute Orientation – Horn's method	Jacobson, 2022	https://www.mathworks.com/matlabcentral/fileexchange/26186-absolute-orientation-horn-s-method, MATLAB Central File Exchange. Retrieved August 31, 2022.
Optimization of parameters of the sigmoid function	Pavao, 2022	https://www.mathworks.com/matlabcentral/fileexchange/42641-sigm_fit, MATLAB Central File Exchange. Retrieved August 31, 2022.
Violin Plots for MATLAB	Bastian Bechtold et al., 2016	https://doi.org/10.5281/zenodo.4559847
Smoothpatch for MATLAB	Yeatman et al., 2012	https://github.com/yeatmanlab/AFQ/blob/master/3Dmesh/smoothpatch_version1b/smoothpatch.m Retrieved August 31, 2022.
Other		
Scanning electron microscope	FEI	Quanta
Scanning electron microscope	FEI	Magellan
Serial block-face in-chamber microtome	Denk and Horstmann, 2004	https://doi.org/10.1371/journal.pbio.0020329
Two-photon laser scanning light microscope	Ramachandra et al., 2020	https://doi.org/10.1038/s41467-020-15672-4

RESOURCE AVAILABILITY

Lead contact

Further information and requests for resources and reagents should be directed to and will be fulfilled by the lead contact, M.H. (mh@brain.mpg.de).

Materials availability

This study did not generate new unique reagents.

Data and code availability

- The raw microscopy image data supporting the current study can be browsed at https://wklink.org/2196 and https://wklink.org/6197 and are available from the corresponding author on request. All annotations are publically available via links listed in the key resources table.
- All original code is publicly available as of the date of publication. DOIs are listed in the key resources table.
- Any additional information required to reanalyze the data reported in this paper is available from the lead contact upon request.

EXPERIMENTAL MODEL AND SUBJECT DETAILS

All experimental procedures were performed according to the law of animal experimentation issued by the German Federal Government under the supervision of local ethics committees and according to the guidelines of the Max Planck Society. Scnn1a-Tg3-Cre mice were purchased from Jackson Laboratory (US) and bred in animal facility at CAESAR institute (Protocol 84-02.04.2014.A331 from the Landesamt für Natur, Umwelt und Verbraucherschutz, Nordrhein-Westfalen, Germany). Male animals between 7 to 10 weeks of age were used in this study.

METHODS DETAILS

Viral injections

The AAV virus (AAV1.CAG.Flex.GCaMP6s.WPRE.SV40) injection was performed on male animals ranging in age from 56 to 72 days. Anesthesia was induced with ketamine and xylazine (120 and 5 mg per kg of body weight, respectively) and maintained using supplementary doses between 10 and 20% of the induction dose whenever the animal began to recover withdrawal reflexes. Through all procedures, body temperature was maintained at around 37°C using a regulated heating blanket and rectal thermal probe. A small craniotomy (approximately 0.5 mm × 0.5 mm) was created at the location of 1.45 mm caudal from bregma and right lateral 3.80 mm, which was 1 mm lateral to the center of the whisker representation in the somatosensory cortex. After removal of dura mater, a long-taper glass pipette (tip beveled at 30°, inner diameter 8–15 μm) filled with the virus stock solution was advanced 1.1 mm towards the midline from cortical surface at an angle of 15° from the horizontal, placing the pipette tip at a depth of 650 μm in the target area. 200 μL virus solution was injected over 5 min. After retraction of the pipette, the skin incision was then closed with Vicryl sutures, and the animals were allowed to recover. Expression time ranged from 14 to 21 days. On the day of Ca^{2+} imaging experiment, animals were again anesthetized with ketamine and xylazine, the skull over the target area (1.45 mm caudal from bregma and right lateral 2.80 mm) was exposed, and a head plate for the stabilization of the head under the microscope was attached. A large craniotomy (approximately 2.5 mm × 2.5 mm) was made, centered on the target area, and the dura mater was opened. Astrocytes were counterstained by applying sulforhodamine 101 briefly to the brain surface and the preparation was stabilized using 1% agarose (Sigma-Aldrich, US, dissolved in artificial cerebrospinal fluid of following composition in mM: NaCl, 135; KCl, 5.4; $CaCl_2$, 1.8; $MgCl_2$, 1; HEPES, 5) and a coverslip to suppress brain movement during multiphoton calcium imaging.

In vivo two-photon calcium imaging with whisker stimulation

Labeled neurons and astrocytes were visualized using a custom-built multiphoton microscope (Ramachandra et al., 2020). Excitation light was provided by a Ti:Sapphire pulsed laser system (Mai Tai, Spectra Physics, CA, USA) tuned to 920 nm. The imaging system consisted of a galvanometric system to generate fast scanning and a 20x objective lens (WPlan-APOCHROMAT, Carl Zeiss, Germany). The barrel field neuropil imaging was carried out at 256 × 256-pixel resolution with a frame rate of 1 Hz. The functional imaging of cell bodies was performed at 64 × 128-pixel resolution with a frame rate of 18.6 Hz. Motion within each frame of the imaging datasets was corrected using red fluorescence from sulforhodamine 101 (Greenberg and Kerr, 2009). The single-whisker stimulation was carried out on the contralateral whisker pad using a piezo-driven plastic pipette tip to generate 15° backward and forward movement of target whisker with 0.5 sec interval. The stimulation was repeated every 8 seconds. At the end of the imaging section, a 2-channel image stack was acquired to register positions of fluorescent cells. The stack contains 600 slices starting from pia towards white matter at a step size of 1 μm and covering an area of 300 × 300 μm^2 at a pixel size of $(1{,}172\ nm)^2$ in-plane.

Extraction of fluorescence signal

The fluorescence $F_{0,t}$ in the t^{th} frame for a given neuron was extracted by calculating the per-frame average of pixel values in a region of interest (ROI). ROIs where manually drawn around the somata of cells in focus. Data from the same neuron over multiple files were linked and analyzed together.

Calculation of ΔF/F0

The baseline fluorescence $F_{0,t}$ was defined as the mean of the lowest 20% of fluorescence values within a window of maximally half of the length of the recording around the t^{th} frame (if not truncated by beginning or end of the file) after applying a Gaussian filter with a standard deviation of 161.28 ms, and $\Delta F/F_{0,t} = (F_t - F_{0,t})/F_{0,t}$.

Spike inference and analyses of stimulus-evoked APs

Spike inference was performed using the algorithm described in (Greenberg et al., 2018), after calibration of the algorithm as described in the same reference but using cell-attached data recorded from four L4 neurons from three Scnn1a-Tg3-Cre mice as described above and using 1 ms bins in the calibration procedure.

For the purposes of determining the timing precision of inferred APs, we selected two groups of measured and inferred APs, with no preceding AP within a window of 1 s. For each of the measured APs, we determined the nearest inferred AP and calculated the temporal distance between the two. We defined differences of less than 250 ms as timing errors and discarded higher differences as detection errors (false negatives). To describe the timing errors, we fit a Laplacian distribution by calculation of the median for the location parameter and the mean absolute distance of data points from the median for the scale parameter from the data.

Stimulus on- and off-responses were defined as all inferred APs in a window of 100 ms around the stimulus onset and offset respectively. Peristimulus time histograms were calculated with 50 ms bin sizes with edges aligned to the stimuli.

Histology

At the end of the imaging experiment, the animals were perfused transcardially with 30 mL 0.15M cacodylate buffer, following at least 90 mL of fixation solution (2.5% paraformaldehyde, 1.25% glutaraldehyde, 2M calcium chloride in 0.08M cacodylate buffer, pH 7.4). After the perfusion, the animal was decapitated and the head was immersed in the same fixation solution at 4°C overnight. For better access to the fixative, the coverslip was removed from the top of the craniotomy window. Extraction of the previously imaged cortical tissue was done on a stereotaxic instrument (Kopf) with modified ear bars to adapt to the animal head plate. A 1 mm diameter biopsy punch (KAI Medical, Honolulu, USA) mounted on an electrode manipulator was centered on top of the target tissue and advanced along cortical axis from cortical surface towards white matter for about 2 mm to cut out the target tissue for *en bloc* EM staining.

Sample preparation for SBEM

En bloc staining for SBEM was performed as in ref.(Hua et al., 2015) with minor modifications. Briefly, the tissue was stained with an osmium tetroxide solution (2% OsO_4 in 0.15M cacodylate buffer, pH 7.4) followed by incubation with 2.5% ferrocyanide (in 0.15M cacodylate buffer, pH 7.4) for 90 min and an additional incubation with 2% OsO_4 solution (in 0.15M cacodylate buffer, pH 7.4) for 45 min. Subsequently, the sample was incubated in saturated aqueous thiocarbohydrazide (TCH) solution for 60 min, 2% OsO_4 aqueous solution for 90 min at room temperature and incubated in unbuffered 1% uranyl acetate (UA) aqueous solution at 4°C overnight. On the next day, the sample was incubated for 2 hours at 50°C in 1% UA aqueous solution and 0.03M lead aspartate solution (pH 5.0). Dehydration and resin embedding were performed with ethanol and acetone, infiltrated with 1:1 acetone and Spurr's resin (Sigma) mixture at room temperature overnight and then with pure resin for 6 hours before baking in a pre-warmed oven at 70°C for 3 days.

Cortical vascular imaging and global alignment

The embedded sample was mounted on an aluminum pin along the cortical axis with conductive epoxy glue (Henkel, Germany) and then trimmed to a cube of $1 \times 1 \times 0.8\ mm^3$. Pia matter was exposed by carefully removing a thin layer of resin with an ultramicrotome (UC7, Leica, Germany) equipped with a diamond-blade (Diatome, Switzerland). The smoothed tissue block was then coated with a 50 nm thin gold layer (ACE600, Leica, Germany), before being imaged in a field-emission SEM (Quanta 250 FEG, FEI) equipped with a custom-built in-chamber ultramicrotome (courtesy of W. Denk (Denk and Horstmann, 2004)). Using 5 keV acceleration energy and 1 μs dwell time, 538 consecutive image planes of dimensions were acquired at a pixel size of 378.9 nm × 378.9 nm and a cutting thickness of 150 nm, resulting in an image stack with a dimension of $1.164 \times 0.776 \times 0.096\ mm^3$. To align the LM imaged C2 barrel in the sample block prepared for 3D EM, a global 3D affine alignment was performed using manually reconstructed cortical blood vessels as landmarks.

Cortical neurite imaging, alignment and correspondence

The sample was then imaged using a field-emission SEM (Magellan, FEI) equipped with a custom-built SBEM microtome (courtesy of W. Denk (Denk and Horstmann, 2004)). Fast continuous imaging mode was implemented by adding piezo actors to operate in line with geared motors (Schmidt et al., 2017). For the acquired dataset, the sample position was centered to the C2 barrel (see above), and acquisition was started in continuous imaging mode for field of views of $229 \times 217\ \mu m^2$ each, separated by motor movements to yield a 2×2 tiling of the $453.2 \times 430.4\ \mu m^2$ region (including overlaps) imaged at 11.24 nm in-plane resolution. Each of these continuously imaged field of views was considered one "motortile" (MT1-4). Subsequently, 12,000 consecutive image planes were acquired, interleaved by microtome cuts set to a cutting thickness of 30 nm, yielding a total extent of the dataset in the cutting direction of 360 μm (Figure 1D). The incident electron energy was 2.8 keV, beam current 3.2 nA and dwell time 100 ns, resulting in a dose of approximately 16 electrons nm^{-2}. The effective data acquisition speed, including movement overheads, was 4.67 M voxel/s. Focus and astigmatism were constantly monitored and adjusted using custom-written autofocus routines.

SBEM image alignment

All images obtained from one image plane and a given motortile (MT, that is, 10 × 7 = 70 images with a size of 2048 × 3072 voxels each) were aligned separately using a custom MATLAB (Mathworks, USA) script based on detected Speeded Up Robust Features (Bay et al., 2008) from the overlap regions of adjacent image pairs (as described in detail for the P25 dataset of ref.(Schmidt et al., 2017)). To match aligned images from consecutive planes, a region with a size of 70% of the horizontal MT size and 50% of the vertical MT size, located at the MT center, was cross correlated with the same region from the next image plane. The translation vector between the cross-correlation peaks was applied to the second image, respectively. In a first alignment, all 12,000 sections were aligned (360 μm in cortical axis) in MT2-4. MT1 was of lower data quality and not further processed. In MT2-4, somata were annotated and dendrites reconstructed for cell type definition. For axon reconstruction and synapse identification, a higher-quality alignment was performed on the first 10,000 sections (300 μm in cortical axis). Here, debris-covered slices were manually detected and excluded from alignment, yielding a total of 9855 slices. After alignment, the 4 resulting 3-D image stacks for each of the 4 MTs of the dataset were each converted to the webKnossos data format (see https://webknossos.org) by splitting the data into data cubes with a size of 128 × 128×128 voxels each. These data were then uploaded to our online data annotation software webKnossos (Boergens et al., 2017) for in-browser distributed data visualization, neurite skeletonization and synapse identification.

Volume and neuron density measurements

The volume of the acquired dataset was 453.2 × 430.4 × 360 μm^3 (each MT was 229 × 217 μm, with overlaps of 4.8 μm and 3.6 μm in x and y direction, respectively). Soma density in the first 300 μm of MTs 2, 3, 4 was on average 110,225 per mm^3. The final 60 μm increased soma numbers by factor 1.178 (slightly lower soma density in beginning of L5A). Together, the entire imaged volume contained 7,598 neurons. Of these, 5,259 were explicitly counted. When including glial somata, neuron fraction was found to be 69.9% and 71.9% in MT2 and MT3, respectively.

Identification of cell types

We identified 1976 cell bodies in the fraction of dataset with optimal staining and image alignment (Figure 1G). For the classification of ExNs and INs, we initially used the size of the cell body and rate of mitochondria in the cytosol to identify INs, which had large and mitochondria-rich cell bodies (n = 127 INs). We then confirmed that these INs had low spine rates along their dendrites. To determine whether any of the small-soma neurons could also be INs, we checked their dendrites and identified another n = 5 cells with low spine rates but small soma size, yielding n = 132 INs total (6.7%). INs frequently had axons that exited from the cell body or from primary dendrites with an orientation towards the pia.

We then determined for all ExNs whether they had an apical dendrite by reconstructing vertically oriented primary dendrites exiting the soma towards the pia. To distinguish between L3 pyramidal and L4 star pyramidal neurons, we determined the cortex depth at which the first fluorescent cell bodies occurred as the beginning of L4 (Figure 1G; quantified post-hoc as the 10^{th} percentile of a sigmoid fit (Pavao, 2022) to the cumulated fluorescent cell bodies along cortical depth based on n = 160 fluorescent somata). To distinguish between L4 star pyramidal cells and L5A pyramidal neurons, we determined the depth at which no more apical-dendrite-free ExNs (i.e., spiny stellates) were found as the beginning of L5A. This was confirmed post-hoc by determining the depth of steepest increase in soma density from white matter towards pia (Figure 1G). 117 somata, positioned outside the barrel, had incomplete dendritic trees and could therefore not be classified; these were excluded from further analysis.

Definition of thalamocortical axons

To identify the axons that were likely originating from the thalamus we used the fact that thalamic axons from VPM have been described to establish large multi-synaptic boutons at high frequency in mouse S1 cortex (Bopp et al., 2017; Motta et al., 2019) (Figure S4A). We applied these criteria and identified 20 such TC axons (Figure 6), entering from the direction of the white matter.

Synapse identification

Synapses were identified by following the trajectory of axons in webKnossos (Boergens et al., 2017). First, vesicle clouds in the axon were identified as accumulations of vesicles. Subsequently, the most likely postsynaptic target was identified by the following criteria: direct apposition with vesicle cloud; presence of a darkening and broadening of the synaptic membrane, indicative of a postsynaptic density; vesicles very close to the membrane at the site of contact. Criteria were similar to those in refs.(Karimi et al., 2020; Schmidt et al., 2017; Staffler et al., 2017). Synapses were marked as uncertain whenever the signs of darkened postsynaptic density could not be clearly identified. All analysis in this study were conducted only on synapses that had been classified as certain. The resulting axonal synapse densities were 0.23 ± 0.50 per μm (TC axons, mean ± s.d., n = 20) and 0.16 ± 0.04 per μm (IN axons, mean ± s.d., n = 18).

Synapse size estimation

A random subset of synapses from TC axons to excitatory cells (n = 17 for StP, n = 40 for SpS) and INs (n = 20 for W-BINs. N = 20 for L-BINs, n = 11 for L4 INs) were used to determine the size of the post-synaptic density (PSD). An expert annotator placed an edge along

the longest dimension of the synapse which was used to estimate the PSD size for comparison across post-synaptic groups (see Figures S4C and S4D).

Definition of barrel volume

To evaluate axonal projections in the context of the cortical column and L4, we needed to define the outlines of the home (C2) barrel. For this, the 3D fluorescence-LM dataset comprising 600 image tiles (256 × 256 voxels each) outlining the C2 barrel was used. Image tiles 320 to 550 were used for barrel surface reconstruction using morphological operations on subsequent image planes. The results were stitched into a global reference frame followed by Gaussian smoothing (kernel 3 × 3 × 3 voxel, s.d. 2 voxels) and curvature weighted smoothing (''smoothpatch'' function from (Yeatman et al., 2012)) to obtain the 3D iso-surface (threshold 0.5) as 3D convex hull. Using a coarse LM-EM transformation based on correspondence points in blood vessels, an affine transformation was computed to convert the LM barrel iso-surface into 3D EM reference space (3 pairs of nodes at bifurcations in blood vessels and 13 pairs of nodes in cell bodies, defined by an expert annotator (using Horn's quaternion-based method (Horn, 1987; Jacobson, 2022). Note that this definition of the barrel (and consequently its lower and upper boundary) was used for all analyses in Figures 2, 3, 4, 5 and 6. The definition of layer borders as a simplified tangential plane (based on fluorescent soma density along the cortical axis, as described above) was only used for Figure 1 to obtain a conservative estimate of cell subtype distributions along the cortical axis (Figure 1G).

Quantitative analysis of axonal projections

Based on the reconstruction of the axonal projection of L4 INs, we calculated the fraction of the axon that was confined to a barrel (''axon barrel ratio'') and the fraction that was confined to L4 (''axon L4 ratio'') (Koelbl et al., 2015). The ''axon barrel ratio'' of the axonal projection was calculated as the ratio between the axonal path length of the L4 IN that was within the home barrel (C2) of the neuron (defined by the barrel iso-surface in EM reference space) and the total axon length. The ''axon L4 ratio'' of the axonal projection was calculated as the ratio between the axonal path length of the L4 IN that was within the L4 borders and the total axon length. The L4 borders (Figure 1G) were defined as described above.

Interneuron subtype definition

INs with axonal path length less than 1.5 mm were excluded from this analysis. Hierarchical clustering (Euclidean distance, Ward's method) was used to determine TC-INs cluster (Figure 2) as well as to separate subtypes within the TC-INs (Figure 3).

Axon diameter measurements

TC axonal diameters (Figure 6H) were reconstructed from three TC axons by measuring the diameters at random locations along its myelinated and unmyelinated trajectory (n = 58, 39 and 32 contour annotations for the three axons, respectively). Contours were traced in the orthogonal viewport most perpendicular to the local axon axis in webKnossos. In case of myelinated segments, the inner unmyelinated axon diameter was measured, and contour was labelled as ''myelinated'' (n = 5, 7 and 5 for the three axons, red dots in Figure 6H inset). In case of branch points the diameter was measured before the branch point. The diameter measurements were linearly interpolated to get the average distribution (bold black curve) shown in Figure 6H. The EM cross sections in Figure 6I were chosen at distances 44 and 122 μm (arrows Figure 6H) for one of the TC axons.

Local cFFI circuit analysis

Local circuit analysis was based on the connectivity data reporting the number of synapses between pairs of neurons or neurites in the dataset. The synaptic connectivity between 3 TC axons, 558 ExNs (175 StP, 383 SpS) and 11 fully reconstructed INs (types whole-barrel, lower-barrel and L4-related) that had their soma in the dataset was analyzed. The connectivity matrix between these neurons was binarized to represent the presence or absence of synaptic connectivity. For each TC axon, all of its excitatory targets were inspected for an additional inhibitory connection from the targeted interneurons by the same TC axon. After excluding excitatory targets with their soma outside the barrel region, the resulting number of cFFI configurations with the additional IN-to-ExN connection were found to be 103 (41 (8 StP and 33 SpS cells), 45 (10 StP and 35 SpS cells) and 17 (5 StP and 12 SpS cells) for the 3 TC axons, respectively) and those without the IN-to-ExN connection were 5 (1 (StP cell), 1 (SpS cell) and 3 (1 StP and 2 SpS cells) for the 3 TC axons), yielding a 95% (92% StP and 96% SpS cells) cFFI ratio (see Figure 6F). When correcting for border effects by excluding excitatory targets near the border of the dataset which limits the complete dendrite reconstruction, the cFFI was found to be 100%. Total synapses from the 3 TC axons to excitatory targets were 59, 53 and 23 and to IN targets were 4, 4 and 9, respectively. Total synapses from all the INs onto excitatory targets were 139, 179 and 50 respectively within the cFFI configurations for 3 TC axons.

Analysis of TC synapse clustering

The axons making TC synapse onto W-BINs and L-BINs were locally checked by an expert annotator for presence of additional synapses onto same dendritic target. This was done for all TC synapses received by W-BINs and L-BINs and used to determine fraction of clustered TC-to-IN synapses.

IN-to-IN connectivity

To determine the IN-to-IN connectome (Figure 4B), all output synapses of the reported INs were inspected with all postsynaptic IN dendrites present in webKnossos, such that any synapse onto any other IN was detected. Therefore, the "zero" entries in the connectome represent no synaptic connection in the dataset. The violin plots (Figures 4D and 4E) were generated using (Bastian Bechtold et al., 2016).

QUANTIFICATION AND STATISTICAL ANALYSIS

All statistical tests were performed using MATLAB and the Statistics Toolbox Release 2021a (MathWorks, USA) and the statistical details of experiments can be found in the figure legends. All tests were done using Wilcoxon-rank-sum test (MATLAB function ranksum) unless otherwise noted.